J. Fluid Mech. (1996), *vol.* 310, *pp.* 139–179

Rayleigh number scaling in numerical convection

By ROBERT M. KERR

Geophysical Turbulence Program, National Center for Atmospheric Research, PO Box 3000, Boulder, CO 80307-3000, USA

(Received 6 November 1992 and in revised form 22 September 1995)

Using direct simulations of the incompressible Navier–Stokes equations with rigid upper and lower boundaries at fixed temperature and periodic sidewalls, scaling with respect to Rayleigh number is determined. At large aspect ratio (6:6:1) on meshes up to $288 \times 288 \times 96$, a single scaling regime consistent with the properties of 'hard' convective turbulence is found for $Pr = 0.7$ between $Ra = 5 \times 10^4$ and $Ra = 2 \times 10^7$. The properties of this regime include $Nu \sim Ra^{\beta_T}$ with $\beta_T = 0.28 \approx 2/7$, exponential temperature distributions in the centre of the cell, and velocity and temperature scales consistent with experimental measurements. Two velocity boundary-layer thicknesses are identified, one outside the thermal boundary layer that scales as $Ra^{-1/7}$ and the other within it that scales as $Ra^{-3/7}$. Large-scale shears are not observed; instead, strong local boundary-layer shears are observed in regions between incoming plumes and an outgoing network of buoyant sheets. At the highest Rayleigh number, there is a decade where the energy spectra are close to $k^{-5/3}$ and temperature variance spectra are noticeably less steep. It is argued that taken together this is good evidence for 'hard' turbulence, even if individually each of these properties might have alternative explanations.

1. Introduction

Two key features of a transition observed in a recent high Rayleigh number convection experiment by Heslot, Castaing & Libchaber (1987) are first that at a given Rayleigh number the normalized heat flux, or Nusselt number (4.3) changed its scaling with respect to Rayleigh number from the classical $Ra^{1/3}$ law to $Ra^{2/7}$; and second that distributions of temperature in the centre of the convective cell changed from Gaussian to nearly exponential. This was not the first time that significant deviations from the classical law have been observed (Chu & Goldstein 1973), but it was the first time that the accuracy of the experiment, control of temperature on the boundary, and the extent of the new regime, from $Ra = 4 \times 10^7$ to 10^{12}, were sufficient to make such a small deviation from the classical law appear plausible. The new scaling regime was called 'hard' turbulence, as opposed to the $Ra^{1/3}$ scaling regime which was designated 'soft' turbulence.

The flow studied by Heslot *et al.* (1987) was gaseous helium at 5 K in a 1 cm diameter, small-aspect-ratio cell. Since the theoretical prediction for the transition to convective rolls assumes infinite aspect ratio (Chandrasekar 1961), a criticism of this experiment has been that the new scaling regime might not be a generic property of convection, but could be related to the effect of the sidewalls. To address this criticism, experiments at different aspect ratios are reported by Wu & Libchaber (1992). In addition, visualizations of similar flows by Zocchi, Moses & Libchaber (1990) and

additional diagnostics have been reported that have allowed some interpretation of the new regime. Some of the new measurements determine temperature fluctuations at different locations in order to provide information on how temperature and velocity scale with Rayleigh number (Sano, Wu & Libchaber 1989; Wu & Libchaber 1992) and how temperature distribution functions vary with location (Castaing *et al.* 1989). The visualizations in a water tank by Zocchi *et al.* have shown that the flow in the hard turbulence regime is characterized by plumes that are pulled from the surface layer by a strong large-scale shear. From these data, phenomenological theories for the transition have been proposed by Castaing *et al.* and Shraiman & Siggia (1990) that predict scaling laws for the dependence of Nusselt number, temperature scales, velocity scales, and boundary-layer length scales. This paper will use the term 'hard' turbulence for the experimental results just quoted and those theoretical predictions that are common to Castaing *et al.* and Shraiman & Siggia.

Another approach to studying the transition to turbulence is direct simulation. In simulations of Rayleigh–Bénard convection with rigid (no-slip) (McLaughlin & Orszag 1982) and stress-free (free-slip) (Curry *et al.* 1984) boundary conditions, some of the experimentally observed transitions in low Rayleigh number convection have been simulated directly. More recently Grötzbach (1982), Domaradzki & Metcalfe (1988), Eidson, Hussaini & Zang (1986), and Moeng & Rotunno (1989) have simulated no-slip convection for Rayleigh numbers up to the order of 400 000. This Rayleigh number is two orders of magnitude less than the Rayleigh number for the transition observed by Heslot *et al.* (1987), but if the effective Reynolds number of convection scales as the square root of the Rayleigh number (since viscosity enters Rayleigh number as a square), the channel flow simulations of Kim, Moin & Moser (1987) suggest that with high-powered numerical methods and extensive computational resources an order of magnitude increase in Reynolds number above the direct simulations just listed, i.e. two orders of magnitude increase in Rayleigh number, is feasible. This would make the Rayleigh number of the simulations roughly comparable to the Rayleigh numbers in water tank experiments (Chu & Goldstein 1973). Even if the simulations cannot simulate a range of Rayleigh numbers sufficient to verify the $Ra^{2/7}$ scaling regime, it would be hoped that with all the physical data available some new insights into the physics behind the transition could be made. The purpose of this investigation is to reach this regime.

Many compromises with the details of the experimental device must be made if a fully three-dimensional turbulent simulation is desired. The most significant difference here will be in the lateral boundary conditions. The original experiment was in an aspect-ratio-one cylindrical cell with rigid boundary conditions on all sides. Current numerical methods are not capable of representing rigid walls in more than one direction if the computational efficiency required to reach high Reynolds numbers is desired. Free-slip sidewalls can be used, as has been done by DeLuca *et al.* (1990), but one possible way of removing sidewalls from consideration is to study only large-aspect-ratio (large-horizontal direction to vertical height) cells. In this case, the type of lateral boundary condition, periodic, free-slip, or rigid, should not affect the scaling if hard turbulence is a generic property of convection. This is currently being checked by introducing free-slip sidewalls for large aspect ratio, with preliminary results reported in Kerr *et al.* (1995). The range of Rayleigh numbers to be discussed is 50 000 to 2×10^7, where the linear instability to convective rolls at large aspect ratio occurs at $Ra = 1708$. Lower Rayleigh numbers are not addressed since the series of transitions up to $Ra = 400\,000$ through periodic rolls, chaotic rolls, and cellular patterns has already been described by Grötzbach (1982) and McLaughlin & Orszag (1982).

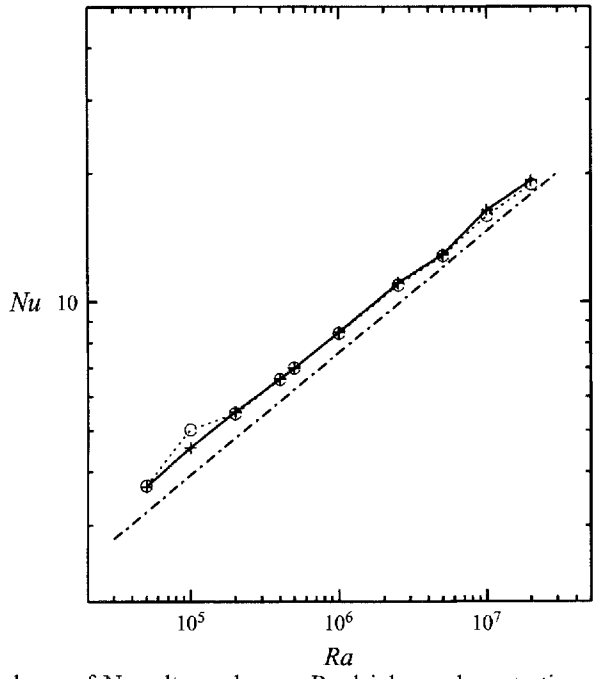

FIGURE 1. Dependence of Nusselt number on Rayleigh number: +, time-average at the walls Nu_w (4.3); ○, time-average of the integral of the normalized heat flux $Nu(z)$ (4.4) (— - —, Wu & Libchaber 1992) $Nu = 0.146Ra^{0.286}$. A least squares fit to Nu at the walls is $Nu = 0.186Ra^{0.276}$.

Surprisingly, by restricting our study to large aspect ratios several advantages appeared. First, it is found that Nusselt number scaling consistent with hard turbulence appears at much lower Rayleigh numbers than in the experimental small-aspect-ratio cell with rigid sidewalls – an observation that has been reported experimentally by Wu & Libchaber (1992). Second, while some improvement in convergence was anticipated from simulating a larger aspect ratio, if this represents a larger ensemble of convection cells, the actual improvement in the convergence of statistical properties of fluctuating statistics, such as the heat flux, at large aspect ratio was more rapid than the larger volume simulated would suggest and significantly fewer convective timescales were required to get good statistics than in low-aspect-ratio experiments (Wu & Libchaber 1992) and simulations (Werne *et al.* 1991). Owing to these fortunate properties of the large-aspect-ratio flow, comparisons with many of the experimental observations and theoretical predictions of scaling of hard turbulence can be made. A plot of Nusselt number versus Rayleigh number for these calculations is shown in figure 1. Two numerical curves are given, one the average of the Nusselt number at the walls (4.3), the other the integral of the averaged normalized heat flux (4.4) across the box, their difference giving an estimate of the error of the statistical sample. This order of error is also found in most of the global and local properties to be reported as discussed in §4.

The experimental comparison in figure 1 is taken from Wu & Libchaber (1992), which like the experiment is large aspect ratio, covers this range of Rayleigh numbers and has the same Prandtl number, 0.7 for a gas. A least-squares fit to Nu at the walls is $Nu = 0.186Ra^{\beta_T}$, where $\beta_T = 0.276 \approx 2/7$, while the experimental results fit $Nu = 0.146Ra^{0.286}$. The experimental claim by Wu & Libchaber (1992) is that their range of Rayleigh numbers is adequate for discriminating between $\beta_T = 1/3$ and $2/7$

for $Nu - 1$, and the results support 2/7. The experiment of Chu & Goldstein (1973) in water, which is again large aspect ratio and covers this range of Rayleigh numbers, but a different Prandtl number 7.0, gives $Nu = 0.183Ra^{0.278}$, which is virtually identical to the simulated curves. It seems that independent of whether the Prandtl number is 0.7 or 7.0, for large aspect ratio magnitudes vary by only 10%.

While the fit in figure 1 suggests confirmation of the 2/7 scaling, Nu versus Ra will not be used as the primary evidence of hard turbulence scaling for these simulations. This is because if one prefers to scale $Nu - 1$ with Rayleigh number, then numerically $Nu - 1 = 0.17Ra^{1/3}$. This is effectively plotted by the thermal boundary layer height in figure 13, showing that the scaling exponent depends strongly on the choice of analysis in this Rayleigh number regime. Instead, extensive analysis of secondary scaling properties, primarily related to boundary layers and more difficult to measure experimentally, will be used to identify the hard convective turbulence regime and to discriminate between the different theoretical explanations for the 2/7 scaling behaviour. It is hoped that once the hard turbulence regime is clearly identified these simulations will be positioned to provide us with important insights into the phenomena of hard turbulence.

The paper is organized as follows. After some discussion of theory, the numerical method, and resolution requirements for these simulations, the analysis will be presented in four parts. The first part will show time-averaged profiles of dynamical quantities in the vertical and the Rayleigh number scaling of boundary layer heights, velocities and temperature. The second part will discuss the vertical velocity skewness, which is important in modelling atmospheric diffusion. The third part will consist of flow visualization with two-dimensional plots and three-dimensional isosurface plots. The fourth part will consist of probability density functions of temperature. Another important piece of analysis is spectra, which will be presented with the discussion of resolution.

2. Theory

The numerical results will be compared primarily with the theoretical predictions of Castaing *et al.* (1989) and Shraiman & Siggia (1990). The primary objective of all these theories is to provide an explanation for the $Nu \sim Ra^{2/7}$ scaling regime. Each makes additional predictions that can be tested by experiments, numerics, or both. Since testing the conflicting theoretical assumptions and predictions is a major objective of these simulations, a short review of the theory seems essential.

The starting point for both Castaing *et al.* (1989) and Shraiman & Siggia (1990) is the following: it is known that in dimensionless variables the kinetic energy dissipation $\dot{E}$ equals $(Nu - 1)Ra$, and the Nusselt number scales as the inverse of a thermal boundary-layer height $Nu \approx 1/\lambda_T$. The classical arguments of Prandtl (1932) and Priestley (1954), reviewed along with more recent references by Castaing *et al.* (1989), predict $Nu \sim Ra^{1/3}$ by making the additional assumption that λ_T is the only small length scale in the problem. The velocity scaling of Deardorff (1970) follows from the classical theory by inserting the classical Nusselt number scaling in (2.4), and the height of any velocity boundary layer and the Kolmogorov length scale $\eta = (\nu^3/\epsilon)^{1/4}$ both scale as λ_T in the classical theory.

In both Castaing *et al.* and Shraiman & Siggia the assumption of one small length scale is relaxed. Instead, relations between a velocity scale, non-dimensionalized as a Reynolds or Péclet number $Pe = ud/\kappa$, λ_T and a temperature scale Δ_c are used to derive new scaling laws. Following the notation of Castaing *et al.*, if power-law

Ref	β_T	ϵ	γ_c	γ_w	β_u	β_z
C	1/3	0.44 = 4/9	−1/9		1/3	
H	2/7	0.43 = 3/7	−1/7		1/7	
SS	2/7	0.43 = 3/7	−1/7			3/7
E1	0.285	0.485	−0.14			
E6	0.286		−0.20			
2D	2/7	0.54	−1/7	−0.064*		
3D	0.28	0.46	−1/7	−1/14	1/7	3/7

TABLE 1. Comparison of scaling exponents from theory, experiment, and simulations. The exponents are defined by equations (2.1)–(2.3) and (2.8): $Nu = d/\lambda_T \sim Ra^{\beta_T}$, $Re = ud/\kappa \sim Ra^{\epsilon}$, $\Delta_c/\Delta \sim Ra_c^{\gamma}$, $\Delta_w/\Delta \sim Ra_w^{\gamma}$, $\lambda_u/d \sim Ra^{-\beta_u}$, and $z^*/d \sim Ra^{-\beta_z}$. References are classical scaling C and hard turbulence scaling H as given by table 1 of Castaing *et al.* (1989); Shraiman & Siggia (1990), SS; experiments for aspect ratio 1, E1, and aspect ratio 6.7, E6, from Wu & Libchaber (1992); the two-dimensional simulations of Deluca *et al.* (1990) and Werne *et al.* (1991), 2D; and the present three-dimensional simulations 3D. Blanks are left where a theory does not make a prediction or there are no experimental or simulated results. * denotes γ_w for the two-dimensional simulations taken from the sidewall temperature exponent. The classical scaling of velocity is consistent with Deardorff (1970).

scaling is assumed the exponents β_T, ϵ, γ_c, β_v, and δ are defined by

$$Nu \approx d/\lambda_T \sim Ra^{\beta_T}, \qquad Pe = ud/\kappa \sim Ra^{\epsilon}, \tag{2.1}$$

$$\Delta_c/\Delta \sim Ra^{\gamma_c}, \qquad \lambda_v/d \sim Ra^{-\beta_v}, \tag{2.2}$$

$$\omega_p d^2/\kappa \sim Ra^{\delta}, \tag{2.3}$$

where ω_p is a characteristic frequency, λ_v is a velocity boundary-layer height, d is the height of the box, and Δ is the temperature difference between the surfaces. The scaling of all of these terms, except ω_p, will be addressed in this paper. Three velocity length scales and two temperature scales will be discussed. The velocity length scales will be compared with the predictions of Castaing *et al.* (2.11) with $\beta_v = \beta_u$, Shraiman & Siggia (2.8) with $\beta_v = \beta_z$, and the Kolmogorov length scale (4.1) with $\beta_v = \beta_\eta$. The two temperature scales and exponents will be based on the temperature in the centre, Δ_c with γ_c, and near the walls, Δ_w with γ_w. Exponents from theory, experiment, two-dimensional simulations, and the three-dimensional simulations to be discussed are summarized in table 1.

To determine relationships between these exponents, a number of simple assumptions have been made. A relation between ϵ and β_T can be obtained by assuming that the dissipation $\dot{E}$ is proportional to the velocity scale cubed divided by a large length scale u^3/d, which is generally believed to be valid for isotropic turbulence and which Shraiman & Siggia (1990) justify for boundary layers. From this and the known dependence of dissipation upon $(Nu - 1)Ra$

$$(ud/\kappa)^3 \sim \dot{E}d^4/\nu\kappa^2 = (Nu - 1)Ra \tag{2.4}$$

and

$$3\epsilon = \beta_T + 1, \tag{2.5}$$

a relation between ϵ, β_T, and γ_c can be obtained by assuming that the vertical velocity and temperature fluctuations are correlated, that is, the heat flux scales as $Pe\Delta_c$ or

$$\epsilon + \gamma_c = \beta_T. \tag{2.6}$$

Both Castaing *et al.* (1989) and Shraiman & Siggia (1990) use relations (2.5) and (2.6).

To solve for β_T, ϵ, and γ_c, one more condition between the velocity and λ_T is necessary. Both Castaing *et al.* and Shraiman & Siggia develop pictures where there is a region above a thermal diffusive layer with a length scale associated with the velocity, but have different views as to the nature of that region. Castaing *et al.* develop a picture of a mixing region and assume that the velocity throughout the central portion of the box is determined by the acceleration of the vertical velocity to the top of a mixing layer. This yields the relation

$$\epsilon + 2\beta_T = 1. \tag{2.7}$$

Shraiman & Siggia calculate how a shear would change the heat flux, concluding that $\lambda_T \sim \tau^{1/3}$, where $\tau = \partial u/\partial z$ is the velocity stress at the wall, and assume that τ depends upon the characteristic velocity of the shear and the characteristic length scale as it would in boundary-layer flows, that is if

$$\left.\begin{aligned} z^*/d = \lambda_v/d = \nu/(u_w d) = \sigma/Pe \sim Ra^{-\beta_z} \\ \text{and} \\ \tau_w d^2/\kappa = (u_w/z^*)d^2/\kappa = Pe^2/\sigma, \end{aligned}\right\} \tag{2.8}$$

then

$$\lambda_T \sim Pe^{2/3}$$

and

$$\beta_T = \tfrac{2}{3}\epsilon. \tag{2.9}$$

Another way of expressing z^* is

$$z^*/d = \lambda_v/d = 2\left[\sigma/(\tau_w d^2/\kappa)\right]^{1/2}. \tag{2.10}$$

Whether relation (2.7) or (2.9) is used, the resulting values for β_T, ϵ, and γ_c are 2/7, 3/7 and $-1/7$.

How does the velocity boundary layer λ_v scale in these theories? An estimate of this scaling is an integral part of the theory of Shraiman & Siggia who predict that $\beta_v = \beta_z = \epsilon = 3/7$. In Castaing *et al.* additional assumptions are made that yield the relation for the height of the mixing layer $d_m/d \sim Ra(\lambda_T/d)^4$ or

$$\beta_v = \beta_u = 4\beta_T - 1 \tag{2.11}$$

and $\beta_v = \beta_u = 1/7$. Another suggestion, known as the Thomae scaling, assumes that the dissipation $\dot{E}$ is proportional to the square of the characteristic velocity divided by the height of the mixing layer $(Re/\lambda_v)^2 \sim (Nu - 1)Re$ or

$$2\epsilon + 2\beta_v = \beta_T + 1. \tag{2.12}$$

This yields a formula for λ_v similar to the definition of the Taylor microscale with $\beta_v = 3/14$. In Shraiman & Siggia the only relation between Re, λ_v, and the dissipation $\dot{E}$ is (2.4).

Both Castaing *et al.* and Shraiman & Siggia assume that $\lambda_v > \lambda_T$, an assumption that is consistent with the scaling of λ_v in Castaing *et al.* and the Thomae scaling, but is not consistent with the scaling of λ_v in Shraiman & Siggia where $\lambda_v = z^*$ decreases faster than λ_T. Based on this Shraiman & Siggia predict a cross-over at very high Rayleigh number from the $Nu \sim Ra^{2/7}$ behaviour to another, as yet undetermined, regime.

3. Equations, boundary conditions, and numerical method

How should the experimental upper and lower boundary conditions be represented numerically? In the experiment of Heslot *et al.* (1987) the upper and lower temperature surfaces were uniform at any given time, but the temperature fluctuated in time to maintain a constant flux. This boundary condition would be feasible numerically, but a minor compromise is to impose a constant temperature at the boundaries at all times. The experimental velocity boundary condition is no-slip or rigid, as opposed to the simplest numerical boundary condition for convection which is free-slip, or stress-free. An important element of the experimental observations and the theoretical explanation of Shraiman & Siggia (1990) is the appearance of shears and a viscous boundary layers. A no-slip boundary condition is necessary to get realistic boundary layers such as observed in channel flow (Kim *et al.* 1987) and for this reason is chosen instead of a free-slip boundary as the velocity boundary condition for this study. Properties common to many turbulent flows, such as exponential distributions, might exist in convection with free-slip boundaries (Sirovich, Balachandar & Maxey 1989; Balachandar & Sirovich 1991), but differences in skewness profiles near the boundaries will support the need for true viscous boundary layers in the dynamics of hard turbulence.

In dimensionless form the equations to be represented are the incompressible Navier-Stokes equations in the Boussinesq approximation between two walls

$$\frac{\partial \boldsymbol{u}}{\partial t} + \boldsymbol{u} \cdot \nabla \boldsymbol{u} = -\frac{1}{\rho_0} \nabla P + T\hat{\boldsymbol{z}} + (1/Re)\nabla^2 \boldsymbol{u}, \tag{3.1}$$

$$\frac{\partial T}{\partial t} + \boldsymbol{u} \cdot \nabla T = \sigma \nabla^2 T, \tag{3.2}$$

$$\nabla \cdot \boldsymbol{u} = 0; \tag{3.3}$$

x and y will be taken to be the horizontal directions and z will be the vertical. The rigid boundary conditions are

$$u = v = w = \frac{\partial w}{\partial z} = 0 \tag{3.4}$$

where w is the vertical velocity. The physical parameter that shall be varied is the Rayleigh number, defined as

$$Ra = \frac{\alpha \sigma g d^3 (T_0 - T_1)}{\nu^2} \tag{3.5}$$

where $\sigma = \nu/\kappa$ is the Prandtl number and T_1 and T_0 are the temperatures at the top and bottom walls. For this study $\rho_0 = 1$, the Boussinesq term $\alpha g = 1$, the height d of the box is 2 (for z running from -1 to 1), $T_1 = 1$, $T_0 = -1$, and $\sigma = 0.7$, the value for air. Rayleigh number was varied by changing the viscosity, which ranged between $\nu = 0.015$ and 0.00075 for $Ra = 5 \times 10^4$ and 2×10^7, all other physical parameters being fixed. The aspect ratio L/d of the horizontal periodicity to the height of the box is 6. Some references to preliminary calculations with smaller aspect ratios and different Prandtl numbers will be made.

While simulation of periodic boundary conditions or free-slip upper and lower boundaries can easily be accomplished with Fourier, sine, and cosine transforms, to simulate rigid upper and lower boundary conditions requires more sophisticated methods to guarantee consistency between the velocity conditions at the walls, the

viscous terms near the walls responsible for the pressure boundary condition, and incompressibility. In addition, because strong vertical shear is concentrated near the boundaries, fine vertical resolution near the walls but less resolution in the interior is desirable. To address these requirements numerically, a Chebyshev method will be used. Some advantages of Chebyshev methods are more resolution near boundaries, a recursion formula for finding derivatives in the function space, and a fast transform (the cosine transform) between Chebyshev and physical space. The recursion formula implies that matrices needed to solve the Poisson equation can be reduced to nearly diagonal forms and solved efficiently and directly in one direction. To use Chebyshev polynomials in more than one direction would create sparse, but full, matrices that would require the use of less direct and more expensive methods. This is the primary reason that numerical work has been confined to Fourier methods in the horizontal.

The Chebyshev method to be used for solving the Poisson equation is based upon divergence-free functions as outlined by Moser, Moin & Leonard (1983) to impose the consistency between boundary conditions (8) and incompressibility (7) in the implicit step. Some advantages of imposing incompressibility are discussed by Thual (1992) for his calculation of zero Prandtl number convection using this code. The divergence-free vector functions use a poloidal–toroidal decomposition to represent the velocity field. This reduces the Stokes terms to second- and fourth-order equations in z. The no-slip conditions are, for the poloidal terms, that the functions are zero at the boundary

$$F_n|_{z=\pm 1} = 0, \tag{3.6}$$

and for the toroidal term that both the value and the first derivative are zero:

$$G_n|_{z=\pm 1} = G_{n,z}|_{z=\pm 1} = 0. \tag{3.7}$$

For the F-functions the combinations of Chebyshev polynomials are

$$F_n = (1 - z^2)T_n. \tag{3.8}$$

For the G-functions the combinations of Chebyshev polynomials are

$$G_n = (1 - z^2)^2 T_n. \tag{3.9}$$

The weight functions that go with these functions are for F

$$P_n = (T_{n-1} - T_{n+1})/2n(1 - \zeta^2)^{1/2} \tag{3.10}$$

and for G

$$Q_n = \left(\frac{T_{n-2}}{n(n-1)} - \frac{2T_n}{(n+1)(n-1)} + \frac{T_{n+1}}{n(n+1)} \right) /4(1 - \zeta^2)^{1/2}. \tag{3.11}$$

Except for the $(k_x, k_y) = (0, 0)$ horizontal Fourier mode, the divergence-free poloidal functions for the velocity are

$$\begin{pmatrix} u \\ v \\ w \end{pmatrix} = \begin{pmatrix} -ik_y \\ ik_x \\ 0 \end{pmatrix} F_n \tag{3.12}$$

and the toroidal functions are

$$\begin{pmatrix} u \\ v \\ w \end{pmatrix} = \begin{pmatrix} k_x \partial/\partial z \\ k_y \partial/\partial z \\ -i(k_x^2 + k_y^2) \end{pmatrix} G_n, \tag{3.13}$$

Ra	t_0	t_f	$\Delta t/\frac{8}{u_c}$	$n_x = n_y$	n_z	Δx	Δz_c	Δz_w	η (4.2)	d/Nu	z^*
5.0×10^4	24	44	0.42	64	32	0.188	0.049	0.0048	0.104	0.54	0.040
1.0×10^5	24	44	0.46	64	32	0.188	0.049	0.0048	0.082	0.44	0.030
2.0×10^5	24	44	0.45	64	32	0.188	0.049	0.0048	0.065	0.36	0.022
4.0×10^5	26	34	0.17	128	48	0.094	0.033	0.0021	0.052	0.30	0.017
5.0×10^5	27	40	0.27	96	48	0.125	0.033	0.0021	0.048	0.29	0.015
1.0×10^6	26	1000	10.0	128	48	0.094	0.033	0.0021	0.038	0.24	0.011
2.5×10^6	26	36	0.18	128	48	0.094	0.033	0.0021	0.028	0.18	0.008
5.0×10^6	49	64	0.21	192	64	0.063	0.025	0.0012	0.022	0.16	0.006
1.0×10^7	28	37	0.14	192	64	0.063	0.025	0.0012	0.018	0.12	0.004
2.0×10^7	24	140	1.25	288	96	0.042	0.016	0.0005	0.014	0.10	0.003

TABLE 2. Simulation statistics: Rayleigh numbers; period used for the statistical samples, first in simulation variables t_0 and t_f, then normalized by $8/u_c$; meshes used the horizontal spacing Δx, the vertical spacing in the centre Δz_c, and the vertical spacing at the wall Δz_w; physical lengthscales – Kolmogorov scale η by (4.2), thermal boundary layer thickness λ_T calculated by d/Nu, and the wall unit z^* calculated by $d \times 2.1 Ra^{-3/7}$ from figure 13.

with the vector weight functions respectively

$$\begin{pmatrix} ik_y/(k_x^2 + k_y^2) \\ -ik_x/(k_x^2 + k_y^2) \\ 0 \end{pmatrix} P_n \tag{3.14}$$

and

$$\begin{pmatrix} k_x/(k_x^2 + k_y^2)\,\partial/\partial z \\ k_y/(k_x^2 + k_y^2)\,\partial/\partial z \\ i \end{pmatrix} Q_n. \tag{3.15}$$

For the $(k_x, k_y) = (0, 0)$ horizontal Fourier mode the two divergence-free functions are $u = F_n, v = w = 0$ and $v = F_n, u = w = 0$ and the weight functions are P_n.

For the temperature, only the F-terms are used to represent constant, zero temperature at the walls, with the temperature difference between the walls represented by a linear gradient. Both the contribution of the linear temperature gradient to the nonlinear advection term in the temperature equation and of the Boussinesq term in the velocity equation are calculated with the full nonlinear terms in physical space.

Using these expansions for the velocity and temperature reduces the matrices to be solved for the Stokes equation and scalar diffusive equations to narrow bands that required minimal time to invert. Dealiasing was accomplished through the 2/3 rule and all mesh sizes will refer to the number of collocation points. Third-order Runge–Kutta using the low-storage scheme of A. A. Wray (private communication) and adapted to a nearly third-order Crank–Nicholson semi-implicit method on the Stokes terms by Spalart, Moser & Rogers (1991) was used for the time advancement. The timestep was chosen at the beginning of each Runge–Kutta cycle using the standard CFL criterion with CFL=1.5, where the linear stability limit for third-order Runge–Kutta is $\sqrt{3}$. Two types of Cray computers were used for these calculations. On a Cray X-MP processor each calculation of the nonlinear terms and the implicit time-advancement required 30 s for a 128^3 mesh, while 6 s of single-processor Cray Y-MP time is required.

The calculations were initialized with random initial conditions on coarse meshes, then run on the coarse mesh until physical profiles and Nusselt numbers developed. Since physical profiles could often be obtained with resolution less than half that

given in table 2 this procedure significantly reduced the computational time required to reach statistical equilibrium. Shortly before the first times given in table 2, the calculations were remeshed by adding additional modes with zero value, then run until the transients associated with remeshing disappeared. Then the calculations were continued to obtain statistical samples.

4. Resolution, statistical sampling, and spectra

A major question when doing direct simulations of fluids is when the resolution can be considered sufficient. It has been shown by Kerr (1985) that in order to resolve all dissipation statistics accurately, at least one decade of the calculation must be dedicated to the viscous regime. This is very expensive and very rarely is this type of resolution used. It is more common to require that the mesh size be the order of the Kolmogorov, or dissipation, length scale

$$\frac{\eta}{d} = \frac{1}{d}\left(\frac{\nu^3}{\epsilon}\right)^{1/4} \tag{4.1}$$

$$= \left(\frac{\sigma^2}{(Nu-1)Ra}\right)^{1/4}. \tag{4.2}$$

It has been shown for channel flow (Kim *et al.* 1987) that if the code is fully dealiased this is sufficient to obtain good, large-scale statistics, and Grötzbach (1983) has shown that the same criterion applies to convection. The Kolmogorov length scale calculated from the data in figure 1 and equation (4.2) gives $\eta/d \approx 1.3Ra^{-\beta_\eta}$ with $\beta_\eta = 0.32$, in agreement with Grötzbach.

Based on these resolution studies, all the calculations to be reported use mesh sizes in the centre of the box within a factor of 2 of the Kolmogorov length scale. Table 2 summarizes the parameters of the simulations to be discussed, including Rayleigh number, time span of the simulations, number of physical space colocation points, and resolution information. To access resolution, three physical length scales that come from the simulations are given to allow comparison with three mesh spacings, maximum and minimum vertical resolution, and the horizontal resolution. The physical length scales are a thermal length scale $\lambda_T = d/Nu$, the Kolmogorov length scale η defined by (4.2), and a wall unit z^* taken from the fit in figure 13. Less resolution is used in the horizontal than vertical in the centre of the box mainly due to the more extreme vertical resolution requirements near the walls, where it is desirable to have resolution based on z^* that is similar to Kim *et al.* (1987).

On the Cray Y-MP it was determined that the largest Rayleigh number that could be adequately resolved was 2×10^7 on a $288 \times 288 \times 96$ mesh for aspect-ratio 6. This calculation was also done on a $192 \times 192 \times 64$ mesh. For $Ra = 2 \times 10^7$, the value of the Nusselt number on the $192 \times 192 \times 64$ mesh was 10% above the value in figure 1 at the walls obtained on the $288 \times 288 \times 96$ mesh. This Nusselt number dependence upon resolution is consistent with Grötzbach (1983). Where these calculations overlap the Rayleigh number regime of earlier calculations, the Nusselt number from these calculations is lower and in better agreement with the experiments than earlier numerical results (Grötzbach 1983; Eidson *et al.* 1986; Moeng & Rotunno 1990).

Since one of the objectives of these calculations is to get statistically independent estimates of scaling variables at each Rayleigh number, a major question is how long

the calculations must be run for variables to converge to statistically independent values. It is desirable to use the shortest period possible, especially at the highest Rayleigh numbers where the calculations are very expensive. There does not seem to exist a generally agreed upon timescale from which estimates can be made. In part this is because, as with the Nusselt number, there is a classical estimate for the convective timescale and a hard turbulence estimate. To measure the true convective timescale would require fine-scale frequency monitoring of the simulation as done by Werne *et al.* (1991), which has not been done for these calculations.

Another measure of determining the convective timescale (J. Werne, private communication) that is consistent with the direct measurement of frequencies in the calculation of Werne *et al.* (1991) is to take the distance around a single roll, $8 = 4 \times 2$ (the height of the box) in these calculations, and divide by the velocity scales. In table 2 the period used for the statistical samples is given in both simulation variables and normalized by $8/u_c$, where u_c is defined in §5. For statistical purposes, dividing by $8/u_c$ might be an underestimate of the number of convective timescales, since a time sequence such as in figure 21 clearly shows several structures containing the largest velocities traversing the box during each convective timescale defined by $8/u_c$.

The $288 \times 288 \times 96$ calculation required 400 hours of single-processor Y-MP time to simulate just one convective timescale. Only one large Rayleigh number simulation was run longer than this, roughly 10 convective timescales for $Ra = 10^6$. The $Ra = 10^6$ calculation was sufficient to achieve good statistical convergence and has been used to make estimates of the errors of all the major statistical quantities determined from the shorter calculations that fill the bulk of the Rayleigh number regime to be discussed. This error analysis supports a conclusion reached early in this investigation that the quantities of primary interest, especially the Nusselt number, converge in the order of 1/10 to 1/4 of the convective timescale $t_c = 8/u_c$, in part due to the large statistical sample achieved by using a large-aspect-ratio box. The errors due to fluctuations obtained from the $Ra = 10^6$ calculation are consistent with the estimate of the errors for the Nusselt number by comparing the Nusselt number calculated at the walls

$$Nu_{\mathrm{w}} = \frac{\overline{\kappa \partial T/\partial z|_{\mathrm{w}}}}{\kappa(T_0 - T_1)/d} \tag{4.3}$$

with the value obtained by integrating the normalized heat flux

$$Nu(z) = \frac{\overline{\kappa \partial T/\partial z} - \overline{wT}}{\kappa(T_0 - T_1)/d} \tag{4.4}$$

across the box, which are both shown in figure 1. Figure 2 shows $Nu(z)$ for $Ra = 2 \times 10^7$. Since one of the primary objectives of this study is to have enough calculations at different Rayleigh numbers to estimate the Rayleigh number dependence of the Nusselt number and search for possible transitions, the rapid statistical convergence of the Nussult number was taken advantage of and most of the calculations were run at full resolution for only a fraction of the convective timescale defined by $t_c = 8/u_c$. Quantities for which statistical errors were obtained are given in table 3. For all of the analysis to follow, the errors in fitting ideal power laws to the results were greater than what the statistical errors of individual quantities would contribute in determining exponents.

One measure of both resolution and the degree of turbulence of a flow is to

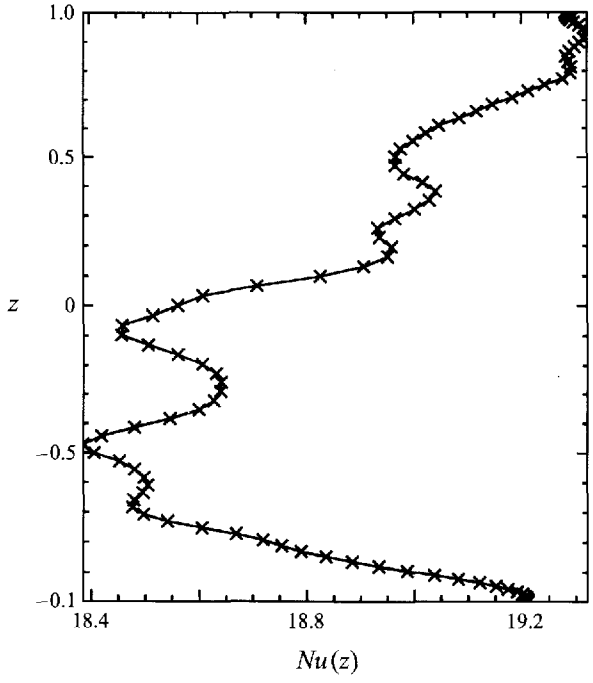

FIGURE 2. Time-averaged normalized heat flux $Nu(z)$ (4.4) for $Ra = 2 \times 10^7$; $\times$ represents vertical grid points.

Quantity	STD	STD for $1t_c$	STD for $0.1t_c$
w_c	4%	2%	
u_c	4%	2%	
Δ_c	5%	3%	
u_w	4%	2.5%	
λ_u	1.5%	0.7%	
Δ_w	1%	0.4%	
λ_T	2%	1.4%	
τ_w	1.6%	1%	
Nu_w	4%	0.5%	1.2%

TABLE 3. Standard deviations of individual times, samples taken over one convective turnover time t_c, and samples taken over $0.1t_c$ for the $Ra = 10^6$ calculation run for $10t_c$. Nu_w is the Nusselt number calculated from the temperature derivative at the walls.

determine the magnitude of the velocity-derivative skewness

$$S_u = -\frac{\overline{(\partial u_i/\partial x_i)^3}}{\overline{(\partial u_i/\partial x_i)^2}^{3/2}} \tag{4.5}$$

which under the assumption of isotropy is equivalent to the normalized vortex stretching rate

$$S_{\omega e \omega} = \frac{2}{35} \frac{\overline{\omega_i e_{ij} \omega_j}}{(\frac{1}{15}\epsilon/\nu)^{3/2}}. \tag{4.6}$$

Moderate Reynolds number simulations (Kerr 1985; Vincent & Meneguzzi 1991) suggest that without buoyant forces, in the Reynolds number range of large numerical

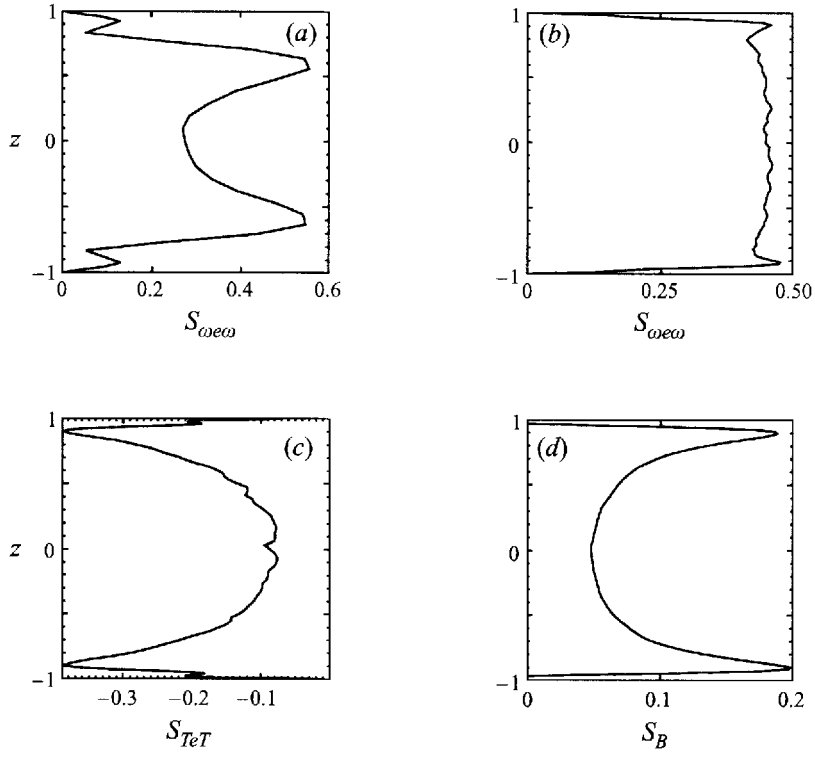

FIGURE 3. Dissipation production terms. Velocity-derivative skewness S_u (4.5) or normalized enstrophy production $S_{\omega e\omega}$ (4.6) at two Rayleigh numbers: (*a*) $Ra = 5 \times 10^4$, (*b*) $Ra = 2 \times 10^7$. (*c*) Temperature dissipation production S_{TeT} (4.8) $Ra = 2 \times 10^7$. (*d*) Enstrophy production by buoyancy S_B (4.7), $Ra = 2 \times 10^7$.

simulations, $S_{\omega e\omega} \approx 0.5$. A flow can be turbulent in this sense for the Taylor microscale Reynolds number R_λ as low as 20 (Herring & Kerr 1982). Without buoyancy, a value of $S_{\omega e\omega}$ much less than 0.5 would suggest that the simulation is either not turbulent or not adequately resolved. In a buoyant fluid, one might expect $S_{\omega e\omega} < 0.5$ because the vortex stretching is normalized by enstrophy produced by both stretching terms and baroclinic terms. R_λ for these calculations ranges between 13 and 66, so examination of the normalized vorticity production terms from vortex stretching and buoyancy should shed light on how turbulent the flow is. Figure 3(*a*) shows that in the lower Rayleigh number simulations of this paper this is exactly the case, at least in the centre of the box. But the high Rayleigh number case behaves more like our expectations for homogeneous, isotropic turbulence. S_u in figure 3(*b*) for $Ra = 2 \times 10^7$ on the $288 \times 288 \times 96$ mesh is approximately 0.45 outside the viscous-diffusion sublayer near the walls, demonstrating both good resolution and turbulent flow. In the centre of the box, the difference between $S_u = 0.45$ and the isotropic expectation that S_u should equal 0.5 could be accounted for by the production of vorticity by buoyancy. The normalized value

$$S_B = \alpha g \frac{2}{35} \frac{\overline{\omega_x T_{,y} - \omega_y T_{,x}}}{(\frac{1}{15}\epsilon/\nu)^{3/2}} \tag{4.7}$$

is shown in figure 3(*d*), and is < 0.1 except near the walls, where the enstrophy production by buoyancy shows evidence of strong boundary effects to be discussed. The temperature dissipation production profile in figure 3(*c*) is discussed below.

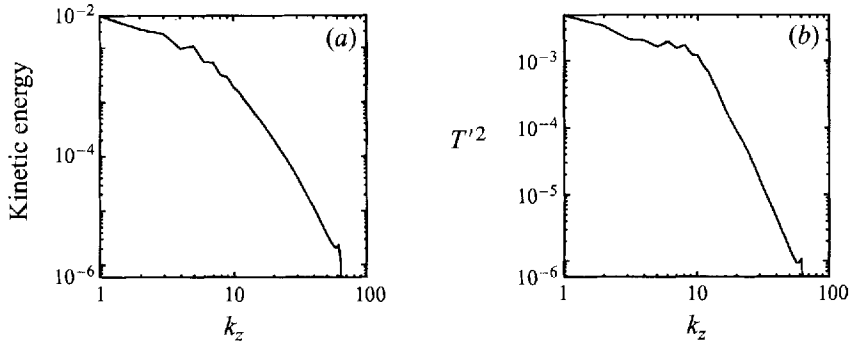

FIGURE 4. Time-averaged Chebyshev distributions for (*a*) kinetic energy and (*b*) temperature variance for $Ra = 2 \times 10^7$.

Using S_u to test resolution is similar to looking at spectra, since the skewness comes from the high-wavenumber end of the spectra. To be well-resolved, spectra should drop significantly at high wavenumbers. In simulations of isotropic turbulence it has been well-established that the high-wavenumber end of spectra should decay exponentially (Kerr 1991) if the simulation is well-resolved. Distributions of Chebyshev polynomials can be used in a similar fashion. In figure 4, time-averaged Chebyshev distributions for the kinetic energy and temperature variance are shown. In figure 5, true horizontal spectra as functions of the horizontal wavenumber $k_h = (k_x^2 + k_y^2)^{1/2}$ are given. The spectra for the individual horizontal components are not given because they are virtually identical to the total energy spectra. The drop in energy at the high modes for the vertical Chebyshev distributions and for horizontal spectra integrated across the box is significant. But the high-wavenumber exponential tails are short. Therefore, a better means of determining whether the resolution is adequate is to look at the vertical velocity spectrum near the wall, which figure 5(*a*) shows has the smallest relative decrease in its value at high wavenumber and therefore could be a more sensitive measure of resolution effects than the other spectra. Even though the value of the vertical kinetic energy is an order of magnitude less than the horizontal kinetic energy at the top of the boundary layer and the integrated horizontal and vertical kinetic energies, comparisons showed that if there was significantly less than a decade drop in the vertical kinetic energy at the top of the boundary layer at high wavenumbers, then contour plots and dissipation profiles show clear signs of numerical noise, S_u is systematically lower, and the Nusselt number is typically 10% or more greater than the experimental values, as was the true for the $192 \times 192 \times 64$, $Ra = 2 \times 10^7$ case noted above.

Besides showing that these calculations are well-resolved, $S_u \approx 0.5$ also shows that the simulations are turbulent. Another indication that the calculations are simulating a turbulent fluid is about a decade of a power-law regime close to $k^{-5/3}$ for the velocity spectra in figure 5(*e*). Spalart (1988) also finds a $k^{-5/3}$ regime up to the highest wavenumber in a simulation with rigid boundaries, but does not have sufficient horizontal resolution to see any fall-off at higher wavenumbers.

In figure 5(*e*), a low-wavenumber kinetic energy spectrum of $k^{-5/3}$ and a high wavenumber spectrum of k^{-3} are given, very reminiscent of theoretical predictions in two-dimensional turbulence of a backwards energy cascade and a forwards enstrophy cascade, with injection of energy and enstrophy at the transition wavenumber (Kraichnan 1967; Batchelor 1969). As will be demonstrated below there is strong two-dimensionality in the flow structures and there is injection of narrow plumes

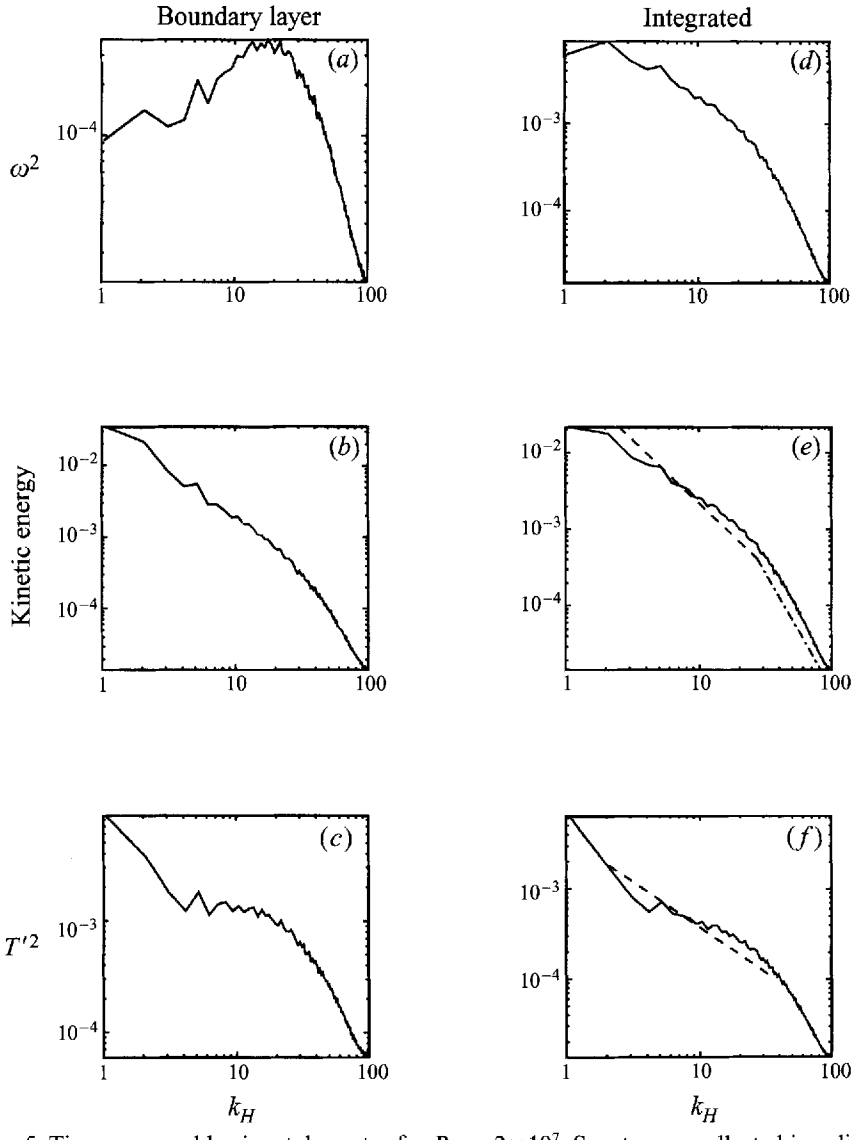

FIGURE 5. Time-averaged horizontal spectra for $Ra = 2\times10^7$. Spectra are collected in cylindrically in planes with $k_h = (k_x^2+k_y^2)^{1/2}$. Minimum wavenumber is $2\pi/6$, where 6 is the lateral dimension of the box. Vertical axes are in simulation coordinates and have not been normalized to be dimensionless as in figures 9 and 10. (*a–c*) Spectra at a plane near the upper wall, $z = 0.92$. (*d–f*) Integrated spectra across the box. (*a, d*) Vertical velocity squared. (*b, e*) Total kinetic energy. (*c, f*) Temperature variance or potential energy. Lines in (*e*) are $-5/3$ (— — —), -3 (— · —). Line in (*f*) is -1 (— — —).

into the interior whose thickness appears to have roughly the correct length scale to be a possible two-dimensional forcing mechanism. To check this possibility, figure 6(*a, b*) plots the flux spectrum, figure 6(*c, d*) plots the temperature variance dissipation spectrum, and figure 6(*e, f*) plots the strain spectrum near the wall and integrated across the box. A strong peak in the flux spectrum is not observed and the temperature variance dissipation and strain spectra do not show any pronounced change at the transition wavenumber between $-5/3$ and -3 behaviour in figure 5(*e*). Thus,

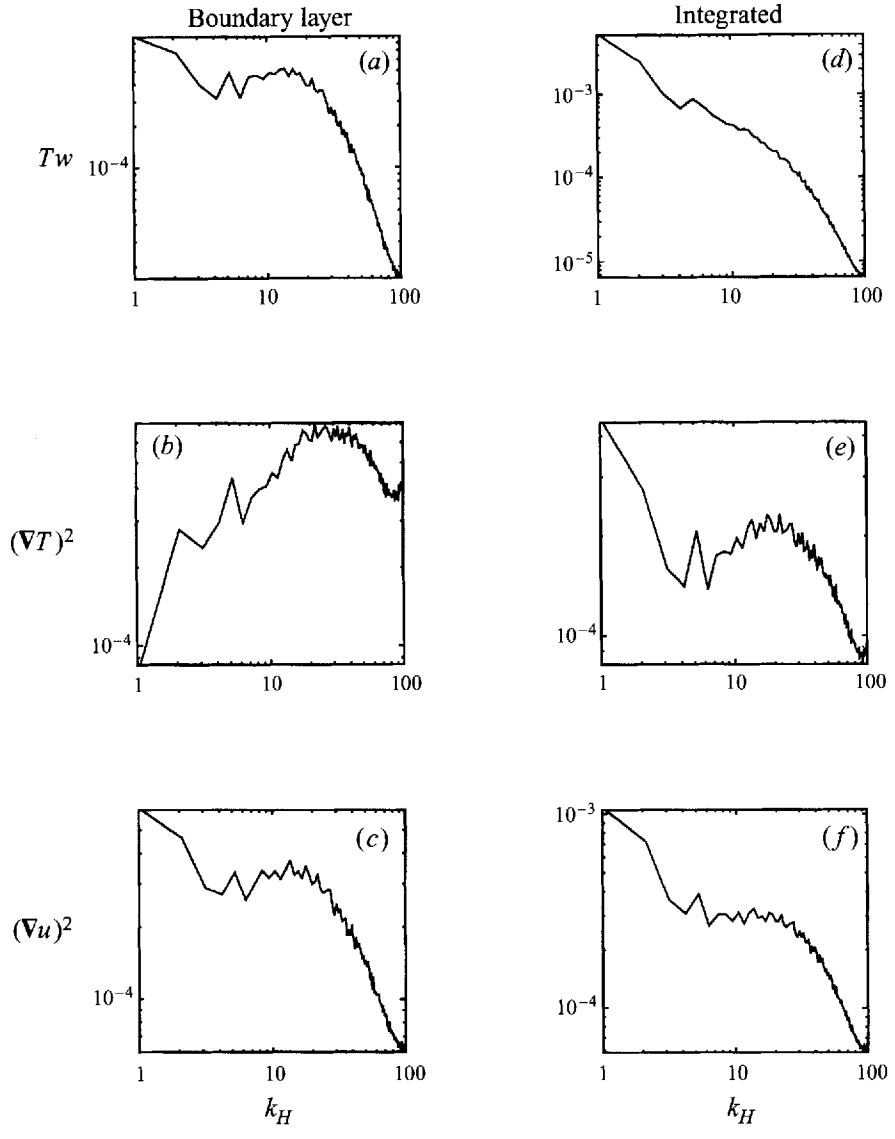

FIGURE 6. Time-averaged horizontal spectra as in figure 5. (*a–c*) Spectra near the upper wall. (*d–f*) Integrated spectra. (*a*, *d*) Heat flux Tw. (*b*, *e*) Temperature derivative squared $(\nabla T)^2$, related to temperature variance dissipation χ by $(\nabla T)^2 = \chi/\kappa$. (*c*, *f*) Strain squared $(\nabla u)^2$. This is related to dissipation ϵ and in isotropic flow is related to the enstrophy $\Omega = (\nabla u)^2 = \epsilon/\nu$.

the two-dimensional mechanism just suggested is not confirmed. Instead, the best interpretation of the kinetic energy spectrum in figure 5(*e*) and enstrophy production profile in figure 3(*b*) might be that while there is a significant non-isotropic convective component, the dynamics can still be largely described by homogeneous, isotropic turbulence. It should be noted that the observation here of a $-5/3$ energy spectrum is consistent with the experimental spectrum in Deardorff & Willis (1985), but is not consistent with a recent experimental determination by Tong & Shen (1992) of velocity structure functions consistent with the Bolgiano $-11/5$ prediction for stratified flow. For now, judgement on these differences will await new calculations being performed to determine Prandtl number effects.

Even though the normalized vorticity production in the centre of the convection box has values consistent with isotropic turbulence, the skewness of the production of temperature variance by the advection terms is very different than the expectation from isotropic studies. Figure 3(*c*) plots

$$S_{TeT} = \frac{2}{15} \frac{\overline{\partial T_i e_{ij} \partial T_j}}{\frac{1}{3}(\overline{\nabla T})^2 \epsilon / 15\nu)^{1/2}} \tag{4.8}$$

which, like the normalized enstrophy production, is 0.5 for passive scalars in isotropic flows. Here it is consistently less than 0.2. It should also be noted that the temperature spectrum in figure 5(*f*) is noticeably less steep, close to k^{-1}, than the isotropic spectrum for passive scalars of $-5/3$. Experimental frequency spectra are also less steep than $-5/3$ (Sano *et al.* 1989). There will be further discussion of temperature spectra in the conclusion, but a complete discussion of the signs of anisotropy in the temperature field will require careful analysis of spectra of all the terms in the temperature variance dissipation equation and will not be discussed here.

5. Vertical profiles and Rayleigh number scaling

Turbulent convection is traditionally divided spatially into thermal boundary layers with steep temperature gradients and a turbulent regime away from boundaries with a small mean temperature gradient. The temperature profile $\overline{T(z)}$ in figure 7 shows these two regions. To investigate the assumptions of Castaing *et al.* (1989) and Shraiman & Siggia (1990) that there should be two boundary-layer length scales, one for the temperature λ_T and one for the velocity λ_v, figures 8–10 show the temperature variance, the r.m.s. velocities, and the energy dissipation for $Ra = 2 \times 10^7$. After some general discussion of these profiles, the Rayleigh number scaling of velocity, temperature, and length scales will be presented in figures 11–13.

From figure 7, one definition of a thermal boundary-layer height can be determined by the gradient of the mean temperature at the wall. Another can be obtained from figure 8, which shows the temperature variance profile $\overline{T'^2} = \overline{(T - \overline{T(z)})^2}$. This profile has its strongest fluctuations near the walls and is nearly uniform across the centre of the box. Two temperature scales are defined, one Δ_c in the centre and the other Δ_w at the peak of the temperature variance profile near the wall. The location of the maximum of T'^2 will be used as the thermal boundary-layer height in figure 13.

Figure 9 shows the vertical profiles of the vertical velocity $w_{rms}d/\kappa$ and horizontal velocity $u_{rms}d/\kappa$ normalized into Péclet numbers for $Ra = 2 \times 10^7$. u_{rms} is taken to be the fluctuating component of the total horizontal velocity

$$u_{rms} = \left[\overline{(u_x - \overline{u_x})^2} + \overline{(u_y - \overline{u_y})^2}\right]^{1/2} \tag{5.1}$$

where both $\overline{u_x}$ and $\overline{u_y}$ are found to be small. Similar profiles, for different Rayleigh numbers, are found for the simulations of Moeng & Rotunno (1990) and the experiments of Deardorff & Willis (1967). The peak of u_{rms} is near the wall and resembles in some ways the classical profile in a shear flow (Kim *et al.* 1987), with a large gradient up to a maximum near the walls and a more gradual decrease up to about half-way towards the centre of the box. The horizontal kinetic energy in the centre of a channel flow is less than half the kinetic energy at the maximum position, while here there is a broad plateau across the centre of the box significantly above one-half the maximum. Despite these differences, the profile of u_{rms} suggests the presence of

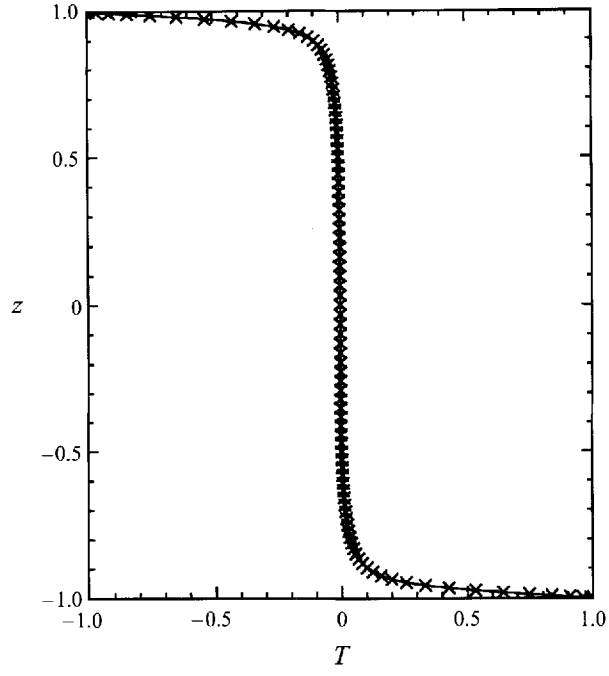

FIGURE 7. Time-averaged temperature profile $T(z)$ for $Ra = 2 \times 10^7$.

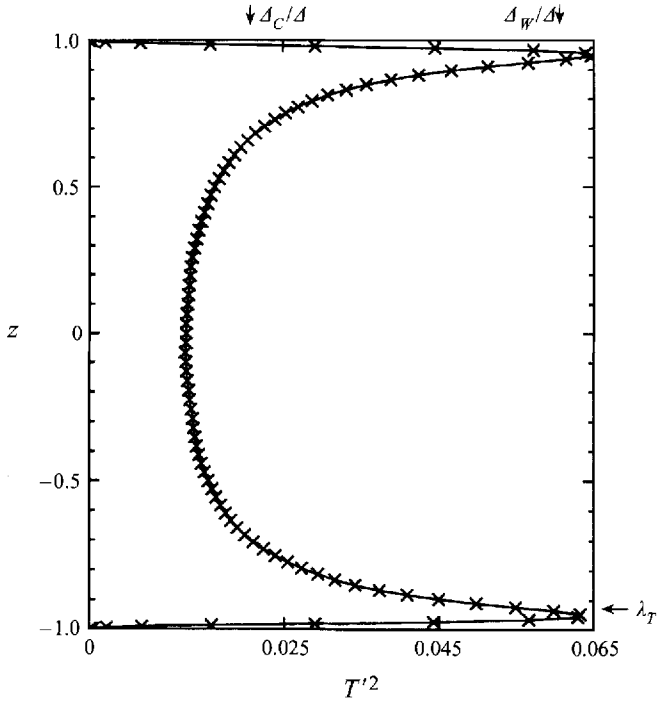

FIGURE 8. Time-averaged temperature variance profile $\overline{T'^2}(z)$ for $Ra = 2 \times 10^7$ in simulation variables. Two temperature scales can be defined, one in the centre Δ_c and another at the peak Δ_w. A definition of λ_T is the location of Δ_w. Arrows indicate sources of temperature and length scales used in figures 11 and 13.

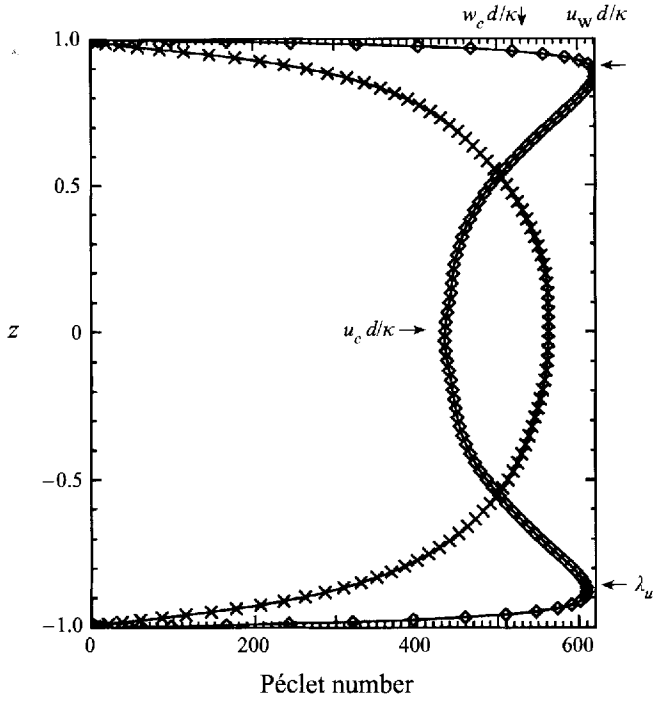

FIGURE 9. Time-averaged normalized velocities for $Ra = 2 \times 10^7$: ◇, horizontal velocity $u_{rms}d/\kappa$. ×, vertical velocity $w_{rms}d/\kappa$. Velocity scales $u_c d/\kappa$, $u_w d/\kappa$ and $w_c d/\kappa$ can be defined from the centre of $u_{rms}d/\kappa$, the peak of $u_{rms}d/\kappa$ and the centre of $w_{rms}d/\kappa$. The velocity boundary layer height λ_u can be defined as the location of u_w. The total kinetic energy, $\frac{1}{2}u_{rms}^2 + \frac{1}{2}w_{rms}^2$ is nearly constant outside the boundary regions. Arrows indicate sources of velocity and length scales used in figures 12 and 13.

shears near the boundaries, which is an assumption of the scaling theory of Shraiman & Siggia (1990). Shears are also indicated by the graphics to be presented in §7. The position of the maximum of u_{rms} will be used as one definition of a velocity boundary-layer height $\lambda_u = \lambda_v$ in figure 13. Two velocity scales (Péclet numbers) that can be determined from the profile of $u_{rms}d/\kappa$ are in the centre $u_c d/\kappa$ and at the maximum $u_w d/\kappa$.

While u_{rms} superficially resembles the horizontal velocity profiles in turbulent boundary layers, w_{rms} behaves very differently than it does in turbulent boundary layers such as Kim *et al.* (1987). In turbulent boundary layers w_{rms} decreases with height above the point of maximum u_{rms}. For convection, w_{rms} increases all the way to the centre of the box, where the characteristic Péclet number $w_c d/\kappa$ is taken. The increase of w_{rms} is less rapid than u_{rms} near the walls, but is still concentrated near the walls with a rounded plateau through the centre of the box. This could be consistent with the picture of Castaing *et al.* (1989) that the vertical velocity accelerates to its value in the centre in a boundary region, but they assume that the acceleration will occur within the thermal boundary layer, not at the height of the velocity boundary layer as indicated by figure 9. The total kinetic energy across the box, $\frac{1}{2}u_{rms}^2 + \frac{1}{2}w_{rms}^2$, is nearly constant with z outside the boundary regions.

Figure 10 plots the kinetic energy dissipation $\dot{E}$ scaled by the energy input from the turbulent heat flux $(Nu - 1)Ra$ for $Ra = 2 \times 10^7$. It is similar to the profile of $\dot{E}$ in Moeng & Rotunno (1990), who plot all the terms in the turbulent kinetic energy budget. This function is just below 1 across most of the box, showing a balance

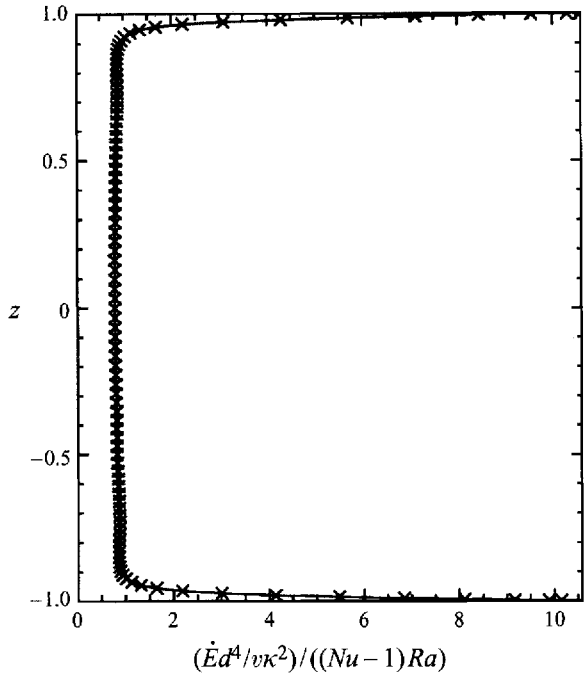

FIGURE 10. Time-averaged, normalized kinetic energy dissipation $(\dot{E}d^4/\nu\kappa^2)/((Nu-1)Ra)$ (2.4). A value just below 1 across the centre shows a near balance between energy input and dissipation. The average wall stress $\tau_w = (\dot{E}_w/\nu)^{1/2}$ (5.2).

between energy input and dissipation. Only near the walls is the dissipation larger, where it increases rapidly. The location at which the dissipation increases rapidly near the walls defines a boundary layer that thins with Rayleigh number. The maximum dissipation at the walls increases with Rayleigh number such that roughly 1/4 of the total dissipation comes from the wall region for all the Rayleigh numbers studied. The wall stress, which is used in equations (2.8) to determine a length scale z^*, is related to dissipation at the walls $\dot{E}_w$ by

$$\tau_w^2 = \dot{E}_w/\nu. \tag{5.2}$$

Based on the locations noted for figures 8 and 9, figures 11 and 12 plot characteristic values for velocity and temperature respectively. These results can be compared with Castaing *et al.* (1989) and Shraiman & Siggia (1990), who make equivalent predictions, to leading order, for how the characteristic velocity and temperature should scale with Rayleigh number. Comparisons can also be made to the measurements by Sano *et al.* (1989) and Wu & Libchaber (1992) and results from the two-dimensional calculations by Werne *et al.* (1991).

The r.m.s. temperature fluctuations Δ_c/Δ in the centre and Δ_w/Δ at the top of the surface layer are plotted in figure 11, where $\Delta = 2$ is the temperature difference across the box. The dashed line for Δ_c/Δ goes as $0.62Ra^{-1/7}$, which is consistent with the theoretical prediction of Castaing *et al.* (1989) and Shraiman & Siggia (1990) that $\gamma = \gamma_c = -1/7$. The two-dimensional simulations of Werne *et al.* (1991) also find $\gamma \approx -1/7$. The dot-dashed curve is the large-aspect-ratio result from Wu & Libchaber (1992) $\Delta_c/\Delta = 1.9Ra^{-0.20}$. (For small aspect ratio Wu & Libchaber (1992) fitted $Ra^{-1/7}$ as shown in table 1.) As a check on the consistency of scales, one can compare the

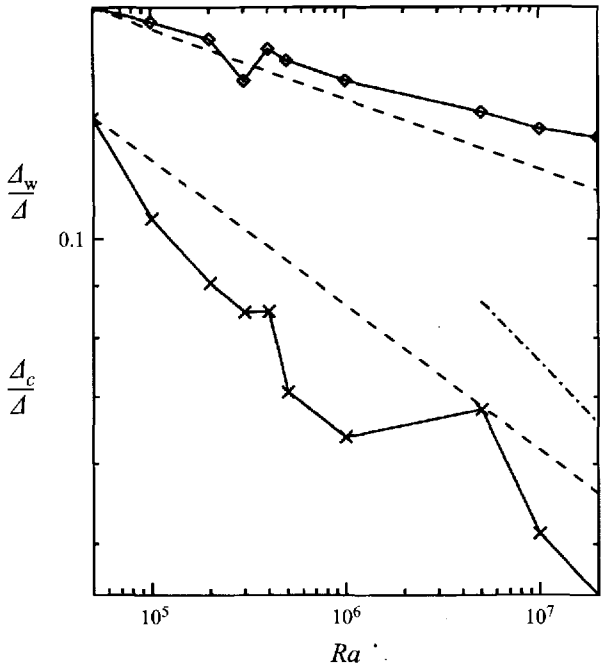

FIGURE 11. Dependence of temperature scales defined in figure 8 on Rayleigh number. ×, Δ_c/Δ; ◇, Δ_w/Δ; — — — through Δ_c/Δ goes as $0.62Ra^{-1/7}$; — — — through Δ_w/Δ goes as $0.37Ra^{-1/14}$; — · — is the large-aspect-ratio result from Wu & Libchaber (1992) $1.9Ra^{-0.20}$.

Nusselt number to the product of the temperature scale and velocity scale to be discussed next. By a Cauchy inequality we know that $Nu - 1 \leqslant (\Delta_c/\Delta)(w_c d/\kappa)$. For these calculations $Nu - 1 = 0.17Ra^{1/3} \approx 0.62Ra^{-1/7} \times 0.27Ra^{0.46}$, suggesting that the turbulent heat flux comes from well-correlated temperature fluctuations and vertical velocity. This is the assumption of equation (2.6).

While the scaling of Δ_c/Δ is roughly in agreement with theory and experiments, Δ_w/Δ behaves quite differently with $\gamma_w = -1/14$ or $\Delta_w/\Delta = 0.37Ra^{-1/14}$ fitting most closely. In both Wu & Libchaber (1992) and Werne *et al.* (1991) the temperature fluctuations near the sidewalls are also significantly less steep than in the centre. This suggests that there might be a relationship between Δ_w determined near the horizontal boundaries in these calculations and the temperature scale determined at the sidewalls in flows with lateral boundaries. This seems plausible if the horizontal boundary layers continue up the sidewalls in those simulations and experiments.

Figure 12 plots $u_w d/\kappa$, $u_c d/\kappa$ and $w_c d/\kappa$, maximum and centreline values of the r.m.s. horizontal and vertical velocities as defined for figure 9. Instead of plotting the theoretical prediction of ϵ using $\beta_T = \frac{2}{7}$ (2.5) to yield $\epsilon = \frac{3}{7} = 0.43 = (\frac{1}{2} - \frac{1}{14})$, two different power laws are shown, one with $\epsilon = \frac{13}{28} = \frac{1}{2} - \frac{1}{28} = 0.46$ following u_w and w_c and the other with $\epsilon = \frac{29}{56} = \frac{1}{2} + \frac{1}{56} = 0.52$ following u_c. u_c increases faster than u_w and w_c at lower Rayleigh numbers, but for $Ra > 5 \times 10^6$ has roughly the same scaling as u_w and w_c. This would suggest that the characteristic velocity should be taken from the curve following u_w and w_c, $0.27Ra^{0.46}$. This is in surprising agreement with the experimental result in figure 1 of Sano *et al.* (1989) for an aspect-ratio-1 cell, $Re = 0.309Ra^{0.485}$. There is no reason to expect such excellent agreement in magnitude since Wu & Libchaber (1992) find experimentally that the Nusselt number

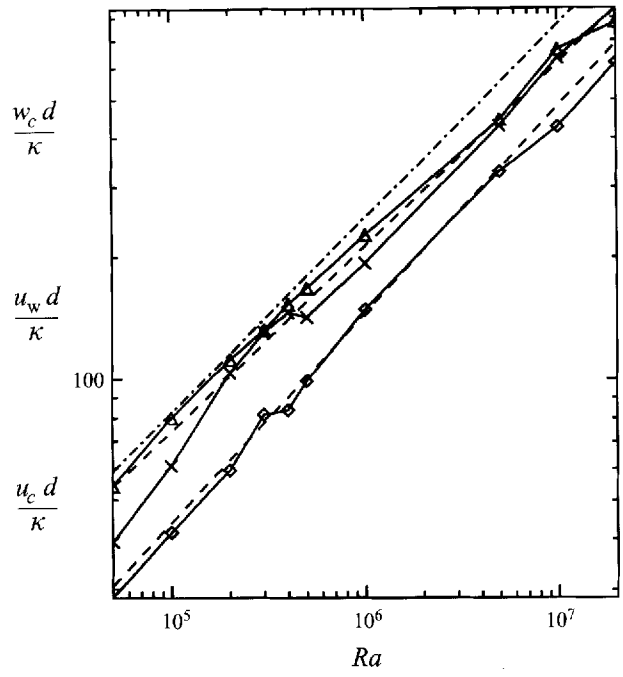

FIGURE 12. Dependence of velocity scales defined in figure 9 on Rayleigh number. +, $u_w d/\kappa$. ◇, $u_c d/\kappa$; △, $w_c d/\kappa$; — — — through $u_w d/\kappa$ and $w_c d/\kappa$ goes as $0.25Ra^{0.46}$; — — — through $u_c d/\kappa$ goes as $0.074Ra^{0.52}$; — - - — is the aspect ratio=1 result of Sano *et al.* (1989) $Pe = 0.309Ra^{0.485}$.

has a strong aspect-ratio dependence, but what might be more significant is that both the simulations and the experiment of Sano *et al.* (1989) find $\frac{3}{7} < \epsilon < \frac{1}{2}$. If $\epsilon = 0.485$ from Sano *et al.* (1989) is used, then (2.6) yields $\gamma \approx -0.20$, which is the large-aspect-ratio scaling law found by Wu & Libchaber (1992). Shraiman & Siggia (1990) suggest that the scaling for Péclet number is greater than $Ra^{3/7}$ due to logarithmic corrections. Note as well that the velocity scaling does not agree with the classical result (Deardorff 1970). This inconsistency between data, both experimental and simulated, and theory will be discussed further in the conclusion.

Figure 13 plots four boundary-layer heights taken from the simulations. Two are taken directly from the position of the maxima of the profiles of temperature T'^2 and velocity u_{rms} in figures 8 and 9 respectively. To improve the statistics, the positions with respect to the upper and lower walls have been averaged and a parabolic fit between mesh points has been used to determine these positions. This averaging and parabolic fitting was also used to determine the maxima of the horizontal kinetic energy and temperature in figures 11 and 12. The two lower curves are indirect measurements of z^* using (2.8),(2.10) that are designed to test the prediction of Shraiman & Siggia (1990). Three curves, $Ra^{-1/7}$, $Ra^{-1/3}$, and $Ra^{-3/7}$, are included to allow comparisons with the theoretical expectations.

Beginning with the thermal length scale λ_T, $Ra^{-1/3}$ – not $Ra^{-2/7}$ – fits this most closely. If λ_T had been taken from the temperature derivative at the wall, it would scale as $1/Nu = Ra^{-2/7}$. Instead, it appears that λ_T defined as the position of the peak of the fluctuation profile scales as $Nu - 1$, which for this range of Rayleigh numbers goes as $Ra^{-0.32}$. If $Nu - 1$ is interpreted as the turbulent contribution to the heat flux coming from vertical velocity and temperature fluctuations, perhaps it

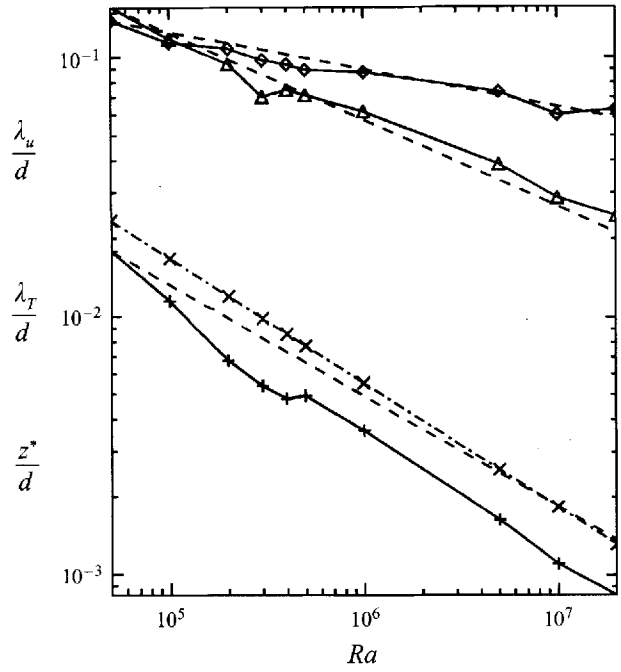

FIGURE 13. Dependence of boundary layer heights on Rayleigh number: △, λ_T/d taken from figure 8; ◇, λ_u/d taken from figure 9; +, $z^*/d = \sigma/(u_w d/\kappa)$ (2.8); — - —, ×, $z^*/d = 2(\sigma/(\tau_w d^2/\kappa))^{1/2}$; — — — through λ_T/d goes as $5.9Ra^{-1/3}$; — — — through λ_u/d goes as $0.65Ra^{-1/7}$; — — through z^*/d goes as $2.1Ra^{-3/7}$.

is not surprising that λ_T taken from the fluctuating temperature profile scales as the fluctuating part of the heat flux.

The velocity boundary layer height λ_u taken from figure 9 is compared in figure 13 with the Castaing *et al.* (1989) prediction $\lambda_v \sim Ra^{-\beta_v}$, $\beta_v = \beta_u = 1/7 = 0.14$. The agreement is excellent, but because λ_u is taken from a fluctuating shear profile this agreement should not be taken as evidence for a mixing layer as proposed by Castaing *et al.* (1989).

The lower two curves representing z^* (2.8),(2.10) superficially match the prediction of Shraiman & Siggia (1990) that the characteristic velocity and the surface stress should be related by a length scale proportional to $z^* \sim 1/Re$ in the same way they would in a turbulent boundary layer. That is, the length scales determined by the velocity scale u_w (2.8) and wall stress τ_w (2.10) scale roughly as $Ra^{-3/7}$, shown by the dashed curve; and a least-squares fit to τ_w yields an exponent of $0.95 \gtrsim 6/7$, the prediction of Shraiman & Siggia (1990). But the assumption of Shraiman & Siggia that $\lambda_v = z^* > \lambda_T$ is violated since z^* is well within the thermal boundary layer. The ratio λ_T/z^* seems too large to be simply accounted for by logarithmic corrections. Furthermore, the largest simulated Rayleigh number $Ra = 2 \times 10^7$ is well below the largest experimental large-aspect-ratio Rayleigh number of 10^{10} in Wu & Libchaber (1992) with $Nu \sim Ra^{2/7}$ scaling. Therefore, one should expect λ_T/z^* to grow even larger for $Ra > 2 \times 10^7$.

There are two other differences between these results and the assumption of boundary-layer scaling by Schraiman & Siggia (1990). First, the position of the maximum of u_{rms} in turbulent boundary layers such as Kim *et al.* (1987) is at about $10z^*$, in wall units. Here λ_u is greater than $10z^*$ at $Ra = 2 \times 10^7$ and the ratio would

be expected to continue growing. Second, the maximum of u_{rms} is $2.5\tau^{1/2}$ in Kim *et al.* (1987), but here $u_w \approx 0.5\tau^{1/2}$ in dimensionless units. These two observations make it unlikely that the profile of u_{rms} for $z \gtrsim z^*$ would be a log layer with the same coefficients as in turbulent boundary layers, as assumed by Shraiman & Siggia (1990). Further work will be necessary to determine how the profile of u_{rms} for $z \gtrsim z^*$ scales with the Rayleigh number.

6. Vertical-velocity skewness

Since the work of Willis & Deardorff (1974) it has been understood that the skewnesses of vertical velocity and of temperature fluctuations need to be accounted for in theories of turbulent diffusion in the atmospheric boundary layer. An example of how the skewnesses are used is the theory for transport asymmetry by Wyngaard & Weil (1991). These theories assume that the vertical-velocity skewness

$$S_w = \frac{\overline{w^3}}{(\overline{w^2})^{3/2}} \tag{6.1}$$

is positive, which is found in measurements of atmospheric convection above heated surfaces by Lenschow, Wyngaard & Pennell (1980), as well as in laboratory experiments by Adrian, Ferreira & Boberg (1986) and simulations by Moeng & Rotunno (1990) with heated lower surfaces and insulating upper surfaces designed to represent aspects of atmospheric convection. Figure 14 shows profiles in z of S_w for three of the Rayleigh numbers simulated here. Unlike the atmospheric situation, where S_w is always positive, S_w for Rayleigh–Bénard convection is negative in the surface layer above the lower surface, correspondingly positive under the upper surface, and nearly zero across the centre of the box. This profile for S_w has been seen before in Rayleigh–Bénard simulations with no-slip surfaces by Eidson *et al.* (1986) and Moeng & Rotunno (1990) and the water-tank experiments of Willis & Deardorff (1974).

Moeng & Rotunno examined the issue in detail. Intuitively one might expect that as localized plumes accelerate above a heated surface they would produce positive S_w. This is what occurs if the upper surface is insulated, where S_w jumps from zero at the boundary to a constant positive value within the surface layer in the simulations of Moeng & Rotunno (1990). They reason that S_w was negative at the lower surface in Rayleigh–Bénard convection because there are plumes of cold, descending fluid that extend between the two surfaces, hitting the lower surface with localized negative velocity that yields negative S_w. At the upper surface an analogous situation occurs, where rising plumes of hot fluid hit the upper surface with localized positive velocity, yielding positive S_w. Another way Moeng & Rotunno look at the problem is to superimpose two cases, one heated at the bottom and insulated at the top and its mirror image, cooled at the top and insulated at the bottom. The resulting superposition S_w yields the profile of S_w seen for Rayleigh–Bénard convection.

Although Moeng & Rotunno (1990) studied only one Rayleigh number, they suggested that as Rayleigh number increases the region of negative skewness would thin. Figure 14 shows this effect, with the region of negative skewness being roughly the same as the boundary-layer thicknesses given in figures 7 to 10. Across the centre of the box the skewness profile appears to be approaching a regime with zero slope and there are no indications that S_w overshoots zero at the top of the boundary. One might question this conclusion since the profile at the highest Rayleigh number, figure 14(*c*) at $Ra = 2 \times 10^7$, is not perfectly smooth. But by plotting the unnormalized

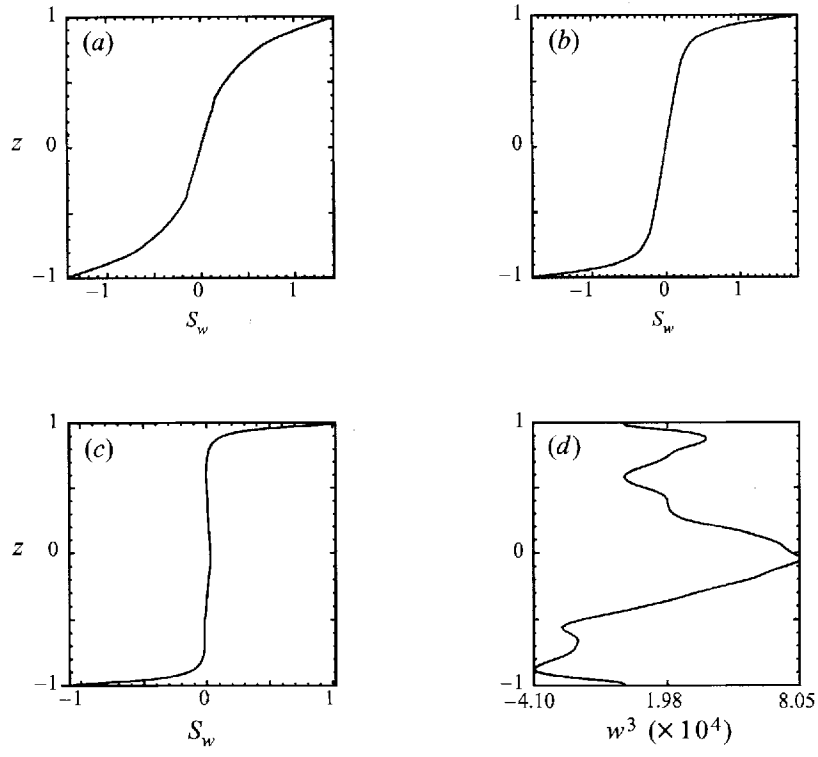

FIGURE 14. $S_w(z)$: (*a*) $Ra = 5 \times 10^4$; (*b*) $Ra = 10^6$; (*c*) $Ra = 2 \times 10^7$; (*d*) w^3, $Ra = 2 \times 10^7$.

vertical velocity cubed, figure 14(*d*) shows that there is no overshoot to opposite values at the top of the boundary layer. Furthermore, what fluctuations there are across the centre are an order of magnitude smaller than the values at any individual time, consistent with using a statistical sample of at least one convective timescale. A rough estimate suggests that it would require a simulation of at least three convective timescales before figure 14(*c*) would not show any discernible fluctuations.

The trend where the thickness of the region of negative S_w decreases suggests that in a high Rayleigh number experiment that could not penetrate the diffusive sublayer, which applies to all atmospheric measurements, negative S_w could never be seen. From this, caution should be used in interpreting the rise in S_w when the upper surface is insulated as in large-eddy-simulations such as in Moeng & Wyngaard (1988). One simulation of Rayleigh–Bénard convection where negative S_w is not seen above the lower surface is the free-slip simulation of Balachandar & Sirovich (1991). It is argued in Schmidt & Schumann (1989) that the sign of S_w in the surface layer changes from positive to negative when there is net kinetic energy transport into the surface layer, which in their large-eddy simulations is associated with increasing the surface roughness. This would be consistent with $S_w > 0$ near the lower boundary in a free-slip simulation, where the absence of a surface boundary layer implies no energy flux into the boundary, and $S_w < 0$ in a no-slip simulation with a surface boundary layer and strong surface dissipation. It will be demonstrated in the next section that incoming plumes and negative S_w could be an important ingredient in producing the shears that are used theoretically to explain hard turbulent scaling. The failure of a free-slip calculation to produce negative S_w could be further evidence for the importance of a true viscous boundary layer in the hard turbulence regime.

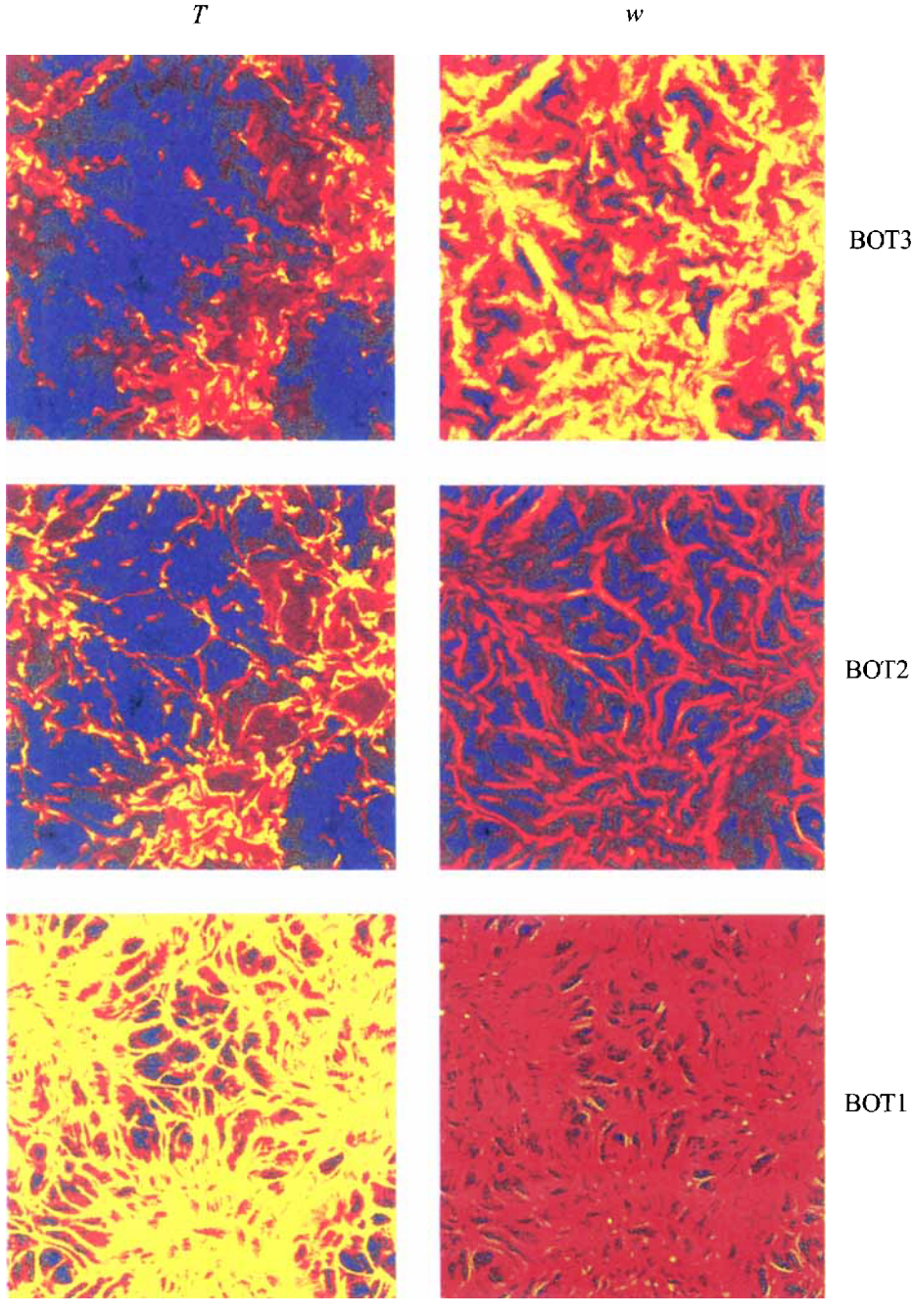

FIGURE 15. Colour contour plots in horizontal planes of the temperature and vertical velocity for $Ra = 2 \times 10^7$ at $Tw_c/8 = 1.47$. Each plot is scaled to its own minimum and maximum. In this figure levels are near the lower surface; BOT1: $z = -0.97$, BOT2: $z = -0.83$, BOT3: $z = -0.61$. Note the dominant convective structure, buoyant sheets leaving surfaces and plumes colliding with the surfaces, producing a cellular pattern with fine networking near the surfaces.

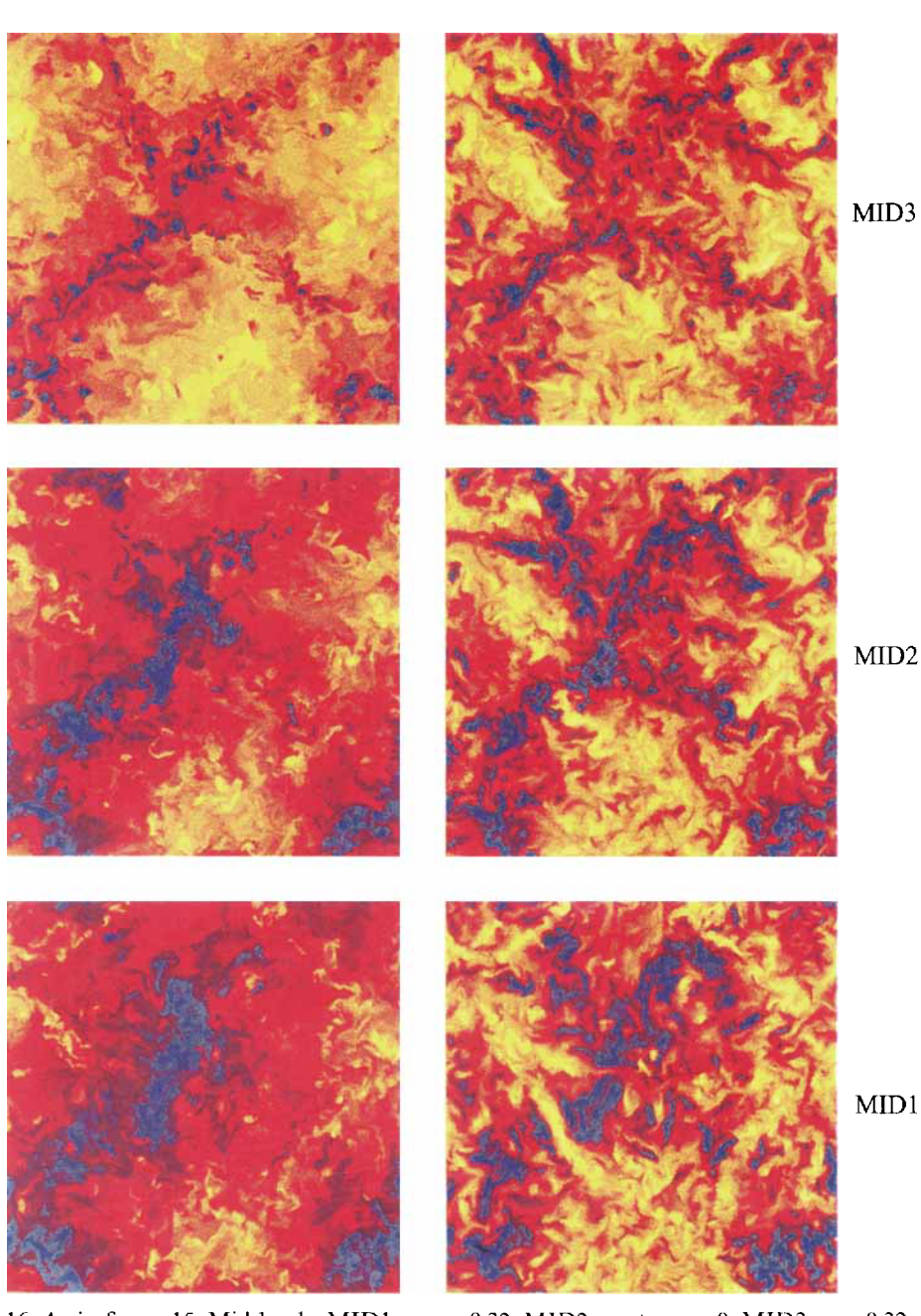

FIGURE 16. As in figure 15. Mid-levels, MID1: $z = -0.32$, MID2: centre $z = 0$, MID3: $z = 0.32$.

7. Flow structures

Figures 15 to 17 show the temperature and vertical velocity near the lower surface, near the mid-plane, and near the upper surface, each with three levels going from bottom to top for one time for $Ra = 2 \times 10^7$. The nine levels are equally spaced in terms of Chebyshev colocation positions at $z = -0.97, -0.83. - 0.61,. - 0.32, 0, 0.32, 0.61, 0.83, 0.97$. Each figure is scaled between the minimum and maxi-

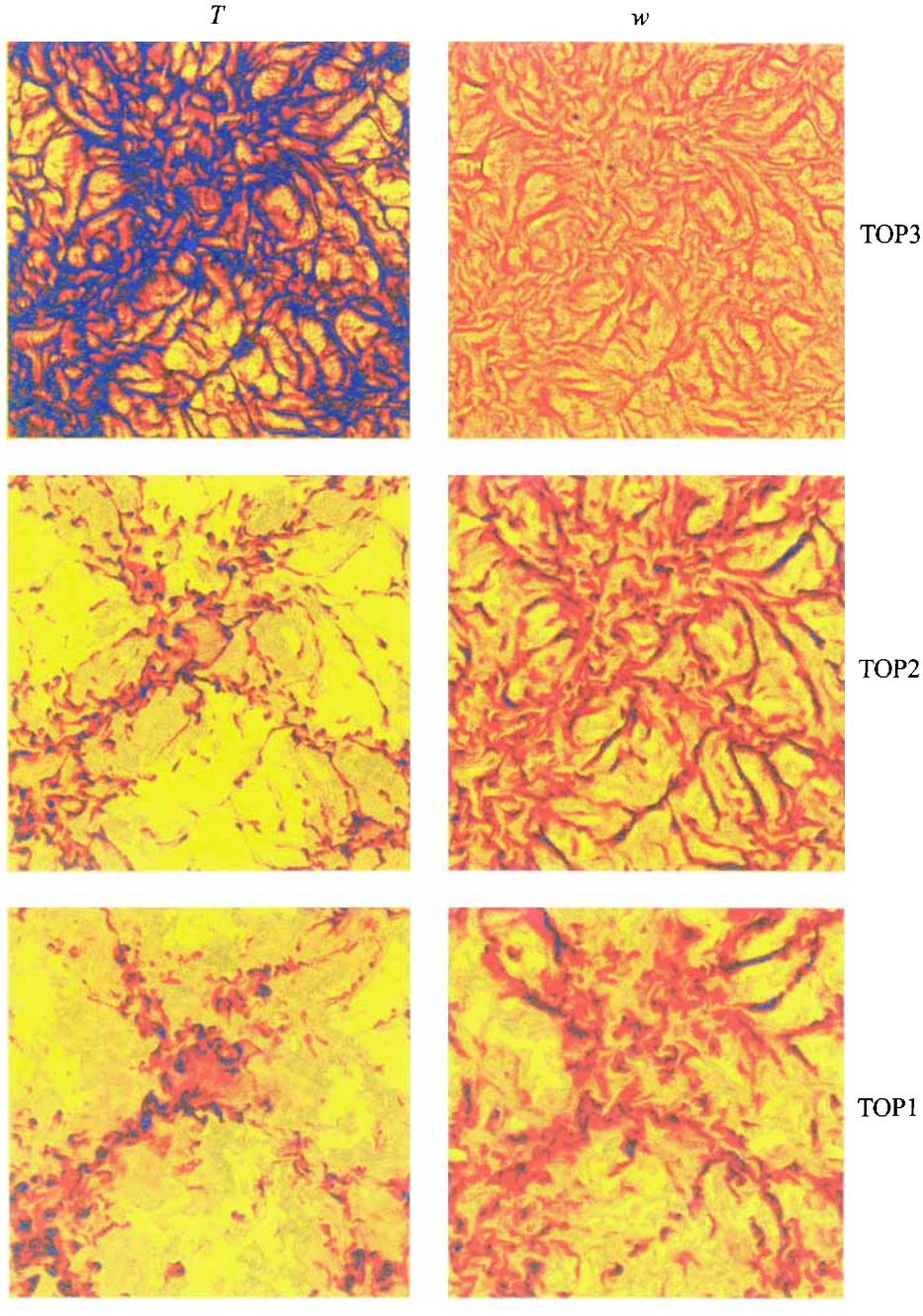

FIGURE 17. As in figure 15. Top levels, TOP1: $z = 0.61$, TOP2: $z = 0.83$, TOP3: $z = 0.97$.

mum of T or w in that figure rather than scaled on global values. Therefore T' rather than T is shown. Plots based on global values were produced, but the rendering shown highlights up- and downdraughts better. These planes were chosen to illustrate the dominant convective structure: buoyant sheets leaving surfaces and plumes colliding with the surfaces, producing a cellular pattern. Several additional features in these plots are worth noting.

First, there are the fine networks near the surfaces, well within both the viscous

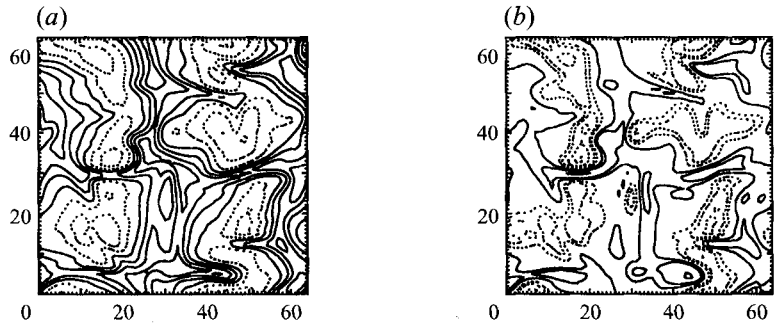

FIGURE 18. Horizontal contour plots half-way from the lower surface. (*a*) Temperature fluctuation $T' = T - \overline{T(z)}$. (*b*) Vertical velocity w. Compare to colour contours for heights BOT3 for $Ra = 2 \times 10^7$ in figure 15. Cell walls become thinner and more intermittent at higher Rayleigh numbers, but the characteristic size of the cellular pattern does not seem to change.

and thermal surface layers, levels TOP3 and BOT1. The networks represent cold and hot sheets leaving the surfaces as downdraughts and updraughts, respectively. At these levels, broader regions of blue in both T' and w at BOT1 and yellow at TOP3 represent plumes penetrating from the opposite surfaces. But the most extreme deviations from the bulk of the vertical motions are small yellow dots in w at level BOT1 and blue dots at level TOP3 of fluid leaving the surfaces. These might be small regions of intense vertical vorticity at these levels. As one moves away from the boundaries to a position just outside both the thermal and viscous surface layers in TOP2 and BOT2, the finest scale networking disappears as strong shears develop from plumes from the opposite surface that hit the surface layers and spread out. Broad expanses of opposite in sign temperature, blue at levels BOT2 and BOT3 and yellow in TOP1 and TOP2, dominate over the finer scale sheets, yellow and orange near the bottom and orange and blue near the top. This mechanism for the generation of strong shear near the surfaces was noted by Moeng & Rotunno (1990). In the regions dominated by small-scale flows away from the walls, there are also more small-scale vertical vortices indicated in the temperature plots by intense blue at level TOP2 and yellow at level BOT2. Similar structures have been observed by Moeng & Rotunno (1990) for $Ra = 380\,000$, and Grötzbach (1982). These networks of sheets are not consistent with the spoke patterns observed by Busse & Whitehead (1974), which extend through the box.

The second feature to note is a dominant alignment at all levels along diagonals that separate the large-scale pattern into two generally upflowing regions staggered between two downflowing regions. This pattern appears for all the Rayleigh numbers simulated, illustrated for the smallest Rayleigh number $Ra = 5 \times 10^4$ in figure 18 and the largest $Ra = 2 \times 10^7$ in figures 15–17, and for all times. Qualitatively, the buoyant sheets thin and become more turbulent as the Rayleigh number increases, but otherwise the large-scale diagonal pattern persists. These large-scale diagonal patterns are very similar to patterns in simulations currently underway (Kerr, Herring & Brandenburg 1995) with impenetrable, free-slip sidewalls where the influence of the geometry is obvious. Test calculations show these patterns appearing once the aspect ratio $L/d \geqslant 3$ and they might be related to large-scale patterns seen up to aspect ratio 12 in water-tank experiments by Krishnamurti & Howard (1981) and Krishnamurti (1995). The pattern therefore appears to be related to the domain geometry and shows the influence of the boundaries, despite periodic side boundary conditions

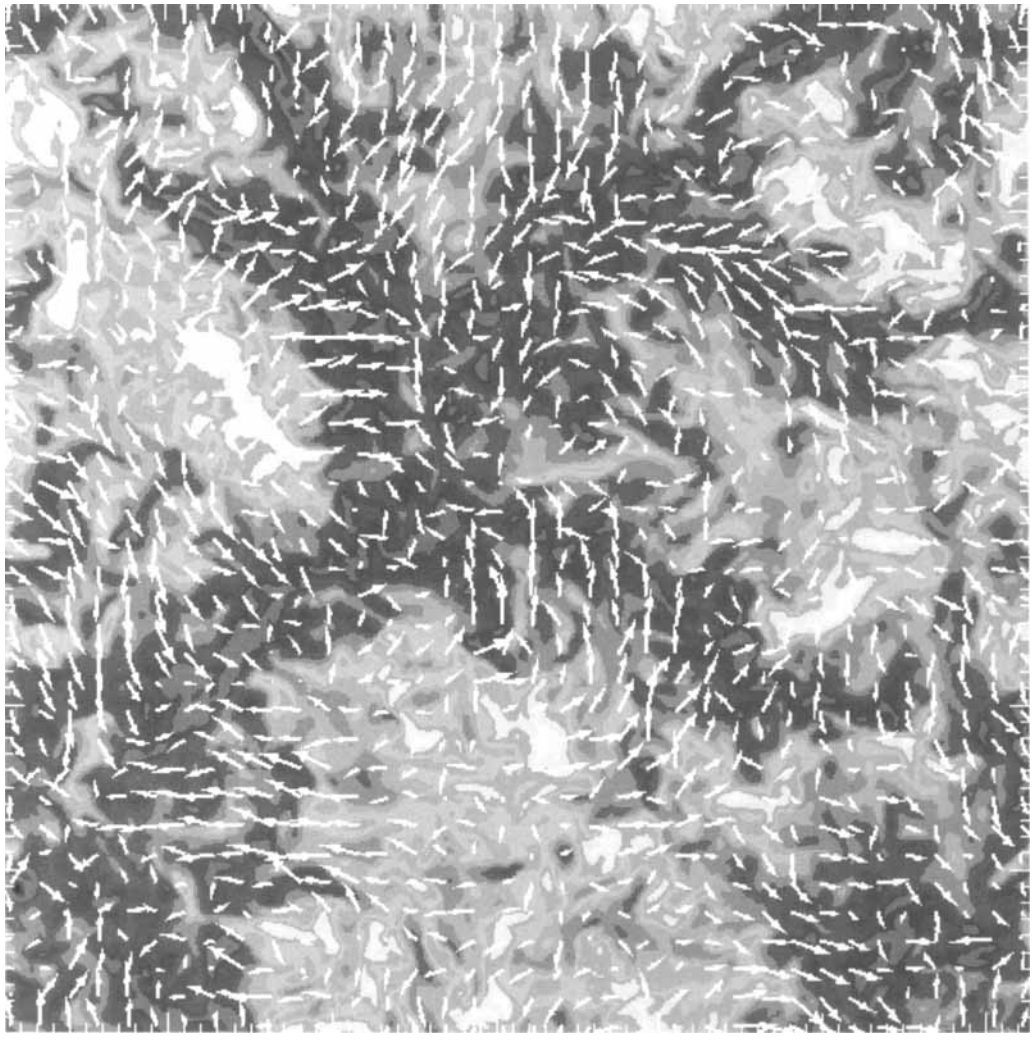

FIGURE 19. Horizontal velocities visualized using arrows indicating strength and direction at level TOP1 $z = 0.61$, near the boundary, overlaying contours of vertical velocity at level MID3 $z = 0.32$.

and the relatively large aspect ratio compared to the most unstable wavelength in linear theory for convection with no-slip boundaries at $Ra = 1708$ of $L/d = 2.016$ (Chandrasekar 1961).

While a large-scale flow, that is a large mean velocity compared to the r.m.s. velocity, is not observed here as in experiments (Krishnamurti & Howard, 1981) and some simulations with impenetrable sidewalls (Werne 1993), there is large-scale organization with respect to the geometry and the aspect ratio is obviously still too small to determine if there is some asymptotic large-scale structure in Rayleigh–Bénard convection. In the atmospheric context, whether there is a maximum size to the cellular pattern and its relationship to boundary conditions has been addressed by large-eddy simulations of Fiedler & Khairoutdinov (1994). Regardless of the influence of the domain size, if the cellular pattern is a result of plumes crossing the box and hitting the surfaces, which is the same mechanism proposed for the production of the boundary-layer shear, then the appearance of the cellular patterns at all the Rayleigh

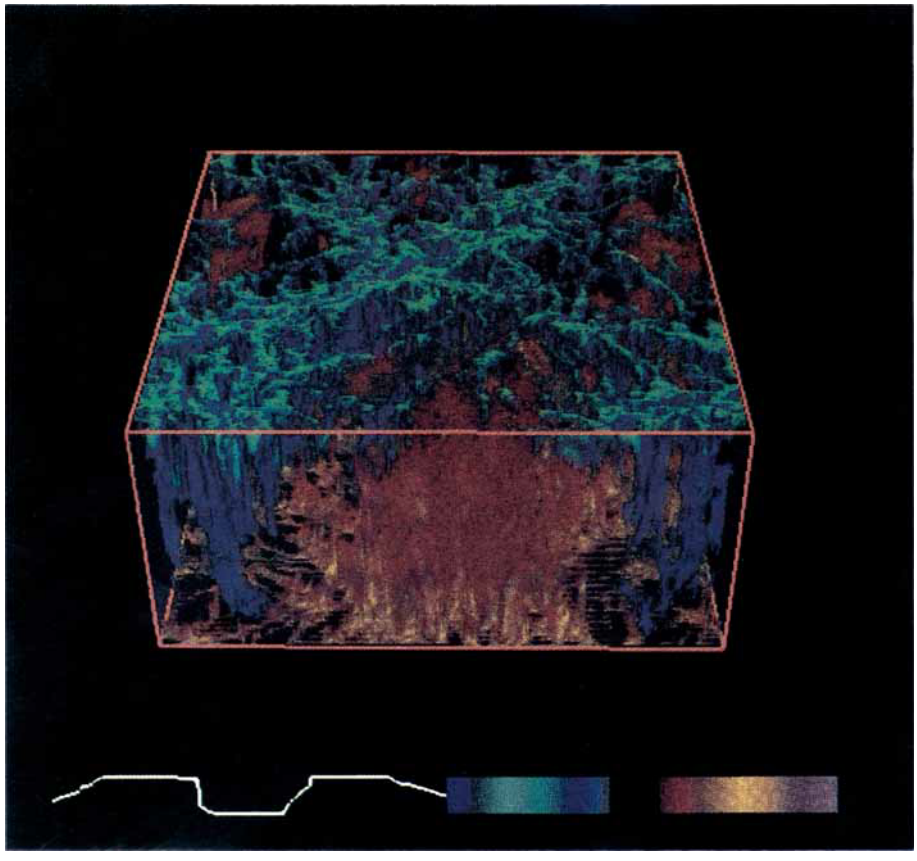

FIGURE 20. Volume rendering of temperature for one time from the $Ra = 2 \times 10^7$ calculation. Note the dominant large-scale diagonal pattern, which persists for all Rayleigh numbers simulated and all times.

numbers simulated also suggests that strong shears that would alter the classical scaling relationships exist for all the Rayleigh numbers simulated.

To illustrate how horizontal velocities in the boundary layer are related to the vertical velocity, figure 19 uses arrows indicating strength and direction for the horizontal velocities overlaying a shaded contour plot for vertical velocity. Levels near the upper boundary are taken, with the level for vertical velocity slightly further from the boundary than the level for horizontal velocities. The dominant feature is strong horizontal velocities coming from regions impacting the surface that converge into the thin sheet-like downdraughts. Similar patterns have been reported by Mason (1989). The relationship between vertical and horizontal velocities just shown suggests a connection between negative S_w and strong horizontal shears at the top of the lower surface layer.

To show to what extent buoyant sheets are seen in the overall flow, figure 20 shows a volume rendering of the temperature field for one time from the $Ra = 2 \times 10^7$ calculation. This figure clearly shows the large-scale cellular pattern extending between the surfaces and the small-scale networking near the surfaces indicated by the x–y slices just discussed.

Figure 21 shows a vertical cross-section of T for 12 times for $Ra = 2 \times 10^7$.

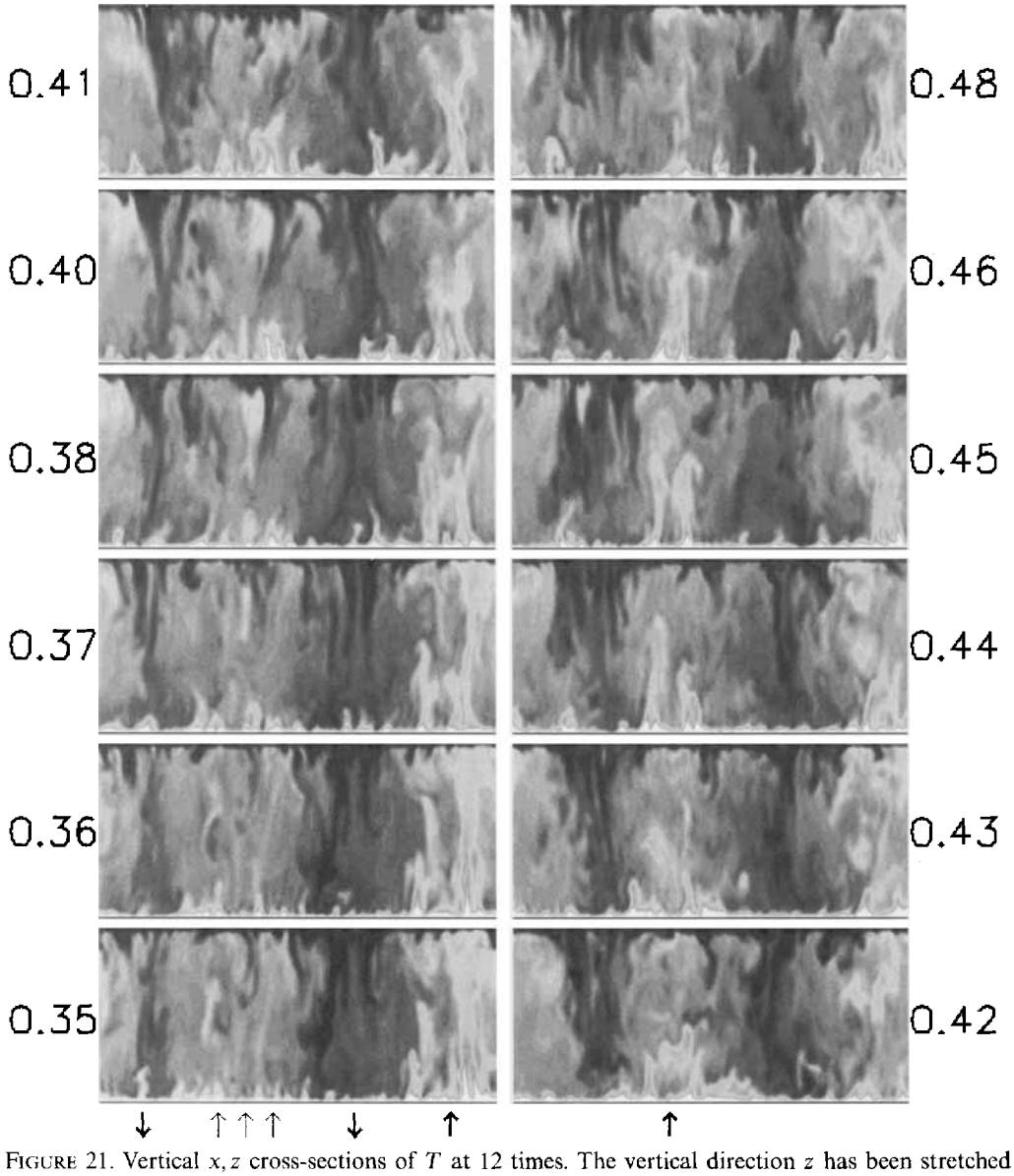

FIGURE 21. Vertical x, z cross-sections of T at 12 times. The vertical direction z has been stretched by a factor of 2. Times run up the column on the left from bottom to top, then up the column on the right, $Tw_c/4d = 0.35, 0.36, 0.37, 0.38, 0.400, 0.41, 0.42, 0.43, 0.44, 0.45, 0.46, 0.48$ The cross-sections are through a line 3/4 from the lower boundary in figures 15–17 and the nearest wall in figure 20, but at much earlier times than those figures. Arrows indicate the following events. At $Tw_c/4d = 0.35$ a hot updraught on the right is indicated. This appears to induce two cold downdraughts, one to the left of the thick up-arrow and one across the periodic boundary at the left edge of the figure. As time progresses small hot updraughts, indicated by three thin up-arrows, develop between the two downdraughts and are swept together to form a single large updraught at $Tw_c/4d = 0.42$ and later times.

The objective is to show a sequence of emerging plumes from the upper and lower surfaces. The sequence starts with a strong, hot, upwelling plume near the right periodic boundary, which seems to induce cold downdraughts as indicated, which in turn sweep together small updraughts into a new strong updraught near the middle

starting near $t = 0.42$. This process occurs at roughly the same location throughout the calculation, consistent with the persistence of the large-scale diagonal structure. In the experiments of Zocchi *et al.* (1990) plumes coming off the surfaces are strongly sheared, which is not observed here. Instead, these visualizations resemble a similar time series in the large aspect-ratio experiment of Chu & Goldstein (1973).

The strong shear above the surface layer in the experiment of Zocchi *et al.* (1990) seems to be related to the strong rotational flow. Comparison of these simulations with preliminary small-aspect-ratio calculations having periodic boundary conditions and $Pr = 0.7$, performed as part of the current investigation, and a wide variety of other simulations mentioned here point to a complex relationship between large-scale shear, rotational patterns and boundary conditions, aspect ratio and Prandtl number. The small-aspect-ratio calculations with periodic boundary conditions suggest a transition to a flow with sheared plumes for L/d below 1.5 to 2. But even for the large-aspect-ratio simulations without a mean shear, an analogy can be drawn with simulations with sidewalls in how strong shears are maintained. In the visualizations of small-aspect-ratio flows with sidewalls showing large-scale flow, reported experimentally by Zocchi *et al.* (1990) and numerically in two dimensions by Werne (1993), a major feature of the dynamics maintaining the large-scale flow is the collision of a surface boundary layer with a vertical wall that produces a flow along the sidewall that hits the opposite horizontal surface and generates new shears. In our calculations with periodic lateral boundary conditions and large aspect ratio, the collisions with the vertical walls could be replaced by collisions between surface layers, with the resulting vertical plumes again hitting opposite walls and driving new surface shears. From this point of view, even when compared to simulations with sidewalls and experiments at low aspect ratio the differences in the overall flow are only apparent; if a portion of these calculations containing half of one roll were compared the flows would look similar. This process of creating new shears is basically two-dimensional and our vertical cross-sections have qualitative similarities to strictly two-dimensional simulations (Werne 1993). This is part of what inspired the suggestion of a two-dimensional analogy for energy spectra in §4 that was not supported by other evidence.

8. Distribution functions

One of the features most stressed in the original hard turbulence experiment of Heslot *et al.* (1987) was how distributions of temperature in the centre plane changed from Gaussian to exponential at the same Rayleigh number that the scaling of the Nusselt number changed from 1/3 to 2/7. Therefore, it is important to report the qualitative dependence of distributions of temperature on Rayleigh number in these simulations. Without an in-depth discussion of resolution dependence and other detailed properties these results should be used in further comparisons with caution.

Figure 22 shows temperature distributions about the midplane for $Ra = 5 \times 10^4$, 10^6, 5×10^6, and 2×10^7. For all of these Rayleigh numbers, a trend towards exponential-like distributions, which is sharper than Gaussian, is indicated. At the lowest Rayleigh numbers the exponential distribution exists upon a broader, nearly Gaussian profile, not shown, that extends to $T = -1$ and 1. To show how close to a true exponential the distribution for $Ra = 2 \times 10^7$ in figure 22 is, figure 23 plots the temperature variance flatness profile

$$F_{T'} = \overline{T'^4}/(\overline{T'^2})^2 \tag{8.1}$$

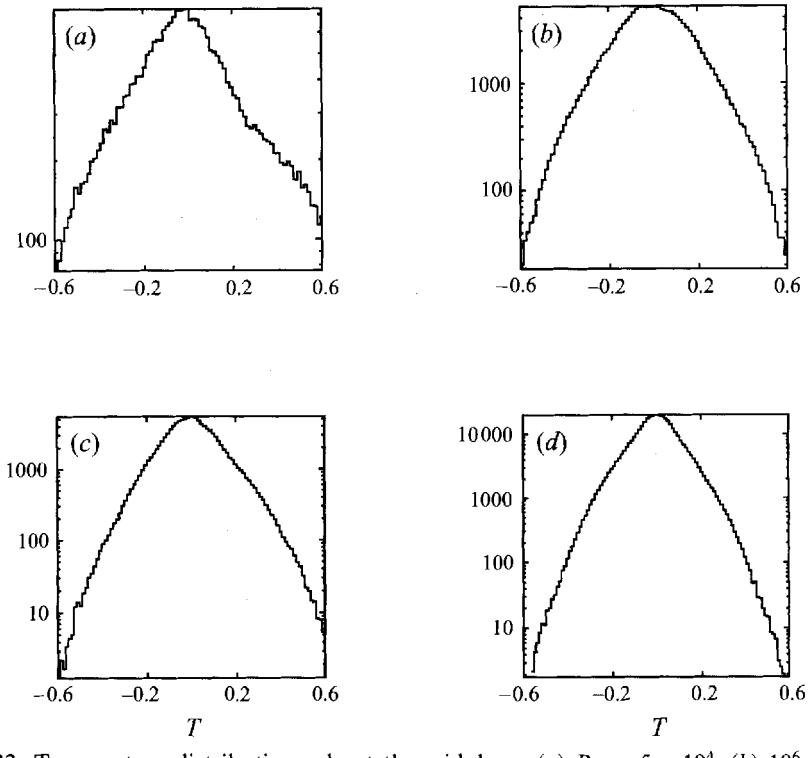

FIGURE 22. Temperature distributions about the midplane. (*a*) $Ra = 5 \times 10^4$, (*b*) 10^6, (*c*) 5×10^6, (*d*) 2×10^7, $-0.29 \geqslant z \geqslant 0.29$. By neglecting broad wings out to $T = -1$ and 1 at lower Rayleigh numbers, exponential distributions in the centre are found in all cases.

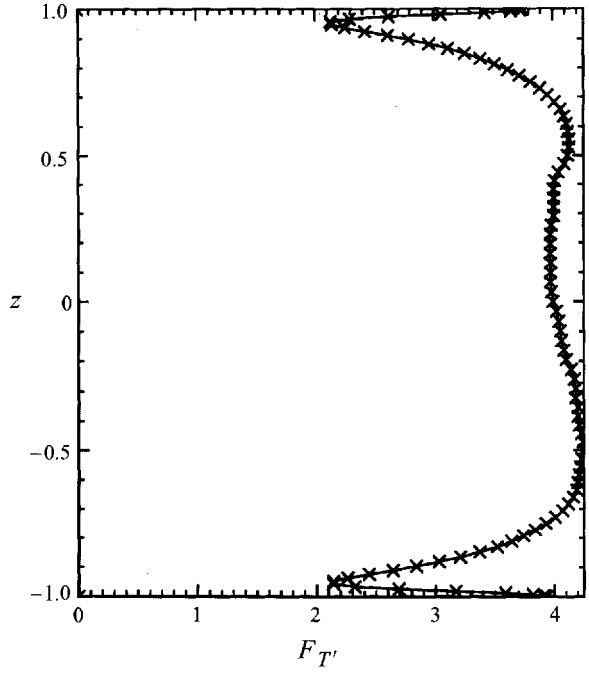

FIGURE 23. Time-averaged temperature variance flatness $F_{T'}$ (8.1) for $Ra = 2 \times 10^7$. $F_{T'} \approx 4.5$ through the centre of the box.

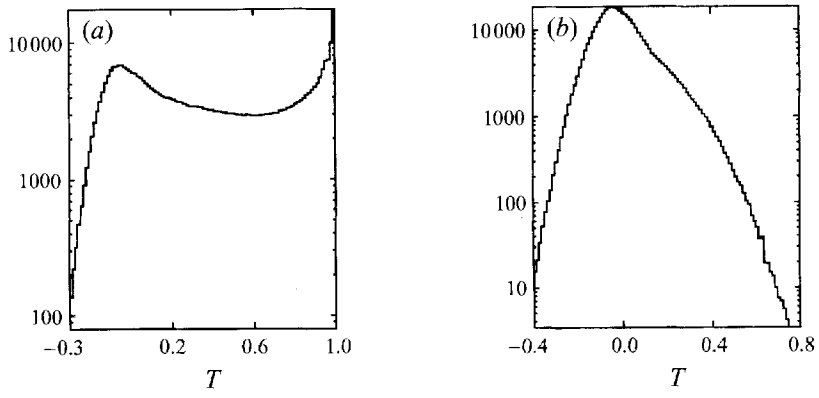

FIGURE 24. Histograms of temperature at different locations for $Ra = 2 \times 10^7$. (*a*) $-0.81 \geqslant z < -1.0$, (*b*) $-0.32 \geqslant z \geqslant -0.79$. $\lambda_T = \pm 0.97$ from figure 8.

for $Ra = 2 \times 10^7$. $F_{T'}$ is roughly 4.5 through the centre of the box, which would place the distribution half-way between a pure Gaussian $F_{T'} = 3$ and a pure exponential $F_{T'} = 6$. While temperature distributions have been useful in identifying the transition to hard turbulence, it is not clear what significance they have in themselves, since they are found in a variety of simulated turbulent flows (Métais & Lesieur 1992).

Besides determining temperature histograms in the centre of the box, Castaing *et al.* (1989) placed a probe near one wall and saw a dependence upon Rayleigh number. By holding the position of the probe fixed and changing the Rayleigh number, Castaing *et al.* also determined how the temperature distributions change with vertical position. This is because, as Rayleigh number increases, the height of the thermal and momentum boundary layers decreases. So, if the probe is within the surface layer at one Rayleigh number, it will be outside it at a higher Rayleigh number. If interpreted in terms of position, the histograms of Castaing *et al.* indicate a trend from negatively skewed temperature (4.8) to positively skewed as the probe moves out from the wall.

With a simulation, histograms of temperature at different locations can be determined directly and are shown in figure 24 for the calculation at $Ra = 2 \times 10^7$. A progression from an extremely non-symmetric distribution within the surface layer in figure 24(*a*), via an intermediate region outside the surface layer in figure 24(*b*), to a symmetric distribution in figure 22(*d*) can be seen. Figure 24(*a*) is for $-0.81 \geqslant z > -1.0$, 24(*b*) is for $-0.32 \geqslant z \geqslant -0.79$, and 22(*d*) is for $-0.29 \geqslant z \geqslant 0.29$ about the midplane, where the peaks of the temperature fluctuation variance in figure 8 are at $z = \lambda_T = \pm 0.97$. The average temperature for the regimes covered by figures 24(*b*) and 22(*d*) is $\overline{T} \approx 0$. So in figure 24(*b*), if the distribution is skewed with one side of $\overline{T} = 0$ having a strong peak, one would expect the other side to have a long tail, as observed. The average temperature $\overline{T}$ in figure 7 at $z \approx \pm 0.91$, the middle of the regime covered by figure 24(*a*), is ± 0.1, so asymmetry with respect to $\overline{T} = 0$ is expected. The peak in figure 24(*a*) just below a value of 1 might represent the intense bright, probably vortical, knots of nearly maximum temperature in figure 15, level BOT2, T', or on the opposite side knots of intense black nearly minimum temperature. It is more difficult to pick these structures out of the frames closer to the walls, levels BOT1 and TOP3, in temperature, but their persistence nearer the walls is suggested by the most extreme deviations in vertical velocity at these levels, the bright yellow dots of w at level BOT1 and blue dots of w at level TOP3.

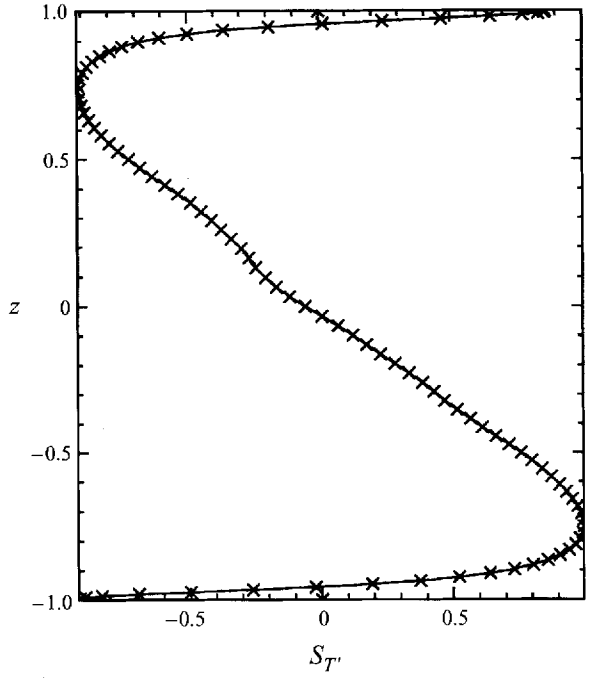

FIGURE 25. Time-averaged temperature variance skewness $S_{T'}$ (8.2) for $Ra = 2 \times 10^7$. $S_{T'}$ is negative in the lower surface layer and positive above it.

Examination of the temperature fluctuation skewness

$$S_{T'} = \overline{T'^3}/(\overline{T'^2})^{3/2} \tag{8.2}$$

in figure 25 can give us some insight into the origin of these non-symmetric distributions. In figure 25 $S_{T'}$ is negative in the lower surface layer and positive above it, before changing sign at the midplane. The region of negative $S_{T'}$ corresponds to the distribution in figure 24(a), and the region of positive skewness corresponds to figure 24(b). In figure 24(a) the temperature distribution within the surface layer is broad with two peaks near $T = 0$ and $T = 1$. T' in figure 24(a) is negatively skewed because there is a negative tail below $T = 0$, but there cannot be a corresponding tail above $T = 1$. But in figure 24(b), outside the surface layer, there is a long positive tail and $S_{T'}$ is positively skewed. As noted, a similar trend from a negatively skewed distribution to a positively skewed one also appears in the experimental result of Castaing *et al.* (1989).

The negative temperature skewness probably has an origin similar to the negative vertical velocity skewness S_w in figure 14 in the sense that both negative skewnesses result from incoming intense plumes dominating the background. Examples of local temperature hot spots within the upper surface layer are shown in figure 15, level BOT1, and figure 17, level TOP3. The origin of the positive skewness above the lower surface layer could be the localized buoyant sheets in levels BOT2 and TOP2. As Rayleigh number increases, the region of negative skewness thins in a manner analogous to the thinning of the negative surface layer of S_w in figure 14. If one accepts the argument presented here and in Moeng & Rotunno (1990) that the source of the anomalous skewness of S_w and $S_{T'}$ in the surface layers is plumes hitting the surface, which in turn leads to strong shears at the top of the surface layer, then

the common trend in the experiments and these simulations for the skewness of the distribution functions would point to the same fundamental mechanism for producing shears in both cases, even though significant differences in the overall flow pattern seem to appear.

For free-slip upper and lower surfaces, distributions near walls in Balachandar & Sirovich (1991) are not as different from the central distributions as the experimental distributions of Castaing *et al.* (1989) or the numerical distributions in figure 24. In particular, with free-slip boundaries $S_{T'}$, like S_w, is probably not negative near the lower wall as in the no-slip simulations and experiments. This would support the conclusion that the surface shears used theoretically to explain hard turbulence scaling require no-slip upper and lower surfaces.

9. Conclusions

Evidence has been presented that for this series of high-resolution simulations of Rayleigh–Bénard convection with large aspect-ratio and periodic boundary conditions, there is evidence for a Rayleigh number scaling regime with the properties of hard convective turbulence. The primary result uses secondary scaling properties to support the existence of scaling consistent with a normalized heat flux, the Nusselt number, going as $Nu \sim Ra^{\beta_T}$ $\beta_T = 0.276 \approx 2/7$, not $1/3$. It could be argued that there is evidence for $Nu - 1 \sim Ra^{1/3}$, but given the excellent agreement of velocity, temperature and boundary-layer depths with experiments and theoretical predictions it appears that if the simulations could be continued to sufficiently high Rayleigh number the $2/7$ dependence for Nusselt number would become stronger. Together with visualizations suggesting the presence of persistent shears and temperature distribution functions similar to experimental observations, the evidence is that the experimental high Rayleigh number regime is being simulated. Although the geometry is significantly different than the original low-aspect-ratio experiment of Heslot *et al.* (1987), many of these scaling laws have also been determined in recent two-dimensional simulations by Werne *et al.* (1991) and large aspect-ratio experiments by Wu & Libchaber (1992). The challenge now is to construct a high Rayleigh number theory that incorporates the low Rayleigh number scaling discussed here that can be extended to higher Rayleigh numbers. Since the boundary-layer scaling indicates no additional cross-overs and because the energy spectrum has developed the characteristic Kolmogorov $-5/3$ power law, there would be nothing inconsistent if such a theory predicted 'hard' turbulence as the asymptotic large Rayleigh number state for convection with no-slip (rigid), constant-temperature upper and lower surfaces.

The experimental visualizations of Zocchi *et al.* (1990) and the scaling theory of Shraiman & Siggia (1990) have previously suggested that boundary layers with shear are part of the dynamics of hard turbulence. The visualizations and scaling laws determined from these numerical simulations also point to the importance of a true viscous boundary layer and no-slip boundary conditions in the dynamics of hard turbulence, even if the large-scale structure of the experimental flows is not reproduced. Important boundary layer effects related to negative vertical velocity and temperature skewnesses at the walls are not produced by the calculations using free-slip surfaces by Balachandar & Sirovich (1991). Evidence for a viscous boundary layer is given in figure 13, which plots length scales calculated from the characteristic velocity and wall stress in the manner suggested by Shraiman & Siggia. The leading-order scaling is very close to what Shraiman & Siggia suggest, even if the details of coefficients and logarithmic corrections they propose are not supported. However, the

length scale defined in this way is within the thermal boundary layer $\lambda_v = z^* < \lambda_T$ with $\beta_z = 3/7 > 2/7 = \beta_T$, not outside it as assumed by Shraiman & Siggia. In a sense this is satisfying because they predict a cross-over to a new type of behaviour at very large Rayleigh numbers based on the Rayleigh number where $z^* < \lambda_T$. Since $z^* < \lambda_T$ is already true, the predicted cross-over should not occur, in agreement with the experiments which suggest that hard turbulence is the only large Rayleigh number state.

If $z^* < \lambda_T$, why is the heat flux suppressed as calculated by Shraiman & Siggia, if one of their primary assumptions is not true? Rather than the viscous boundary layer smoothly advecting the thermal boundary layer and modifying the heat flux as Shraiman & Siggia suggest, intermittent dynamics similar to those above the viscous sublayer in a turbulent boundary layer could be playing some role in the dynamics within the thermal boundary layer in hard turbulence. It could be that the second velocity boundary-layer height λ_u identified in figures 9 and 13 plays a role. λ_u was identified from the profile of the horizontal velocity u_{rms} and could be tied to sheared boundary layers by the relationship of the peak of u_{rms} to the wall stress (2.8),(2.10). Castaing *et al.* (1989) predicts a mixing length height without invoking boundary layers that has the same scaling as λ_u with $\beta_u \approx 1/7 < 2/7 = \beta_T$.

If hard turbulence is the asymptotic high Rayleigh number state, what of the common belief that the large Rayleigh or Reynolds number state of a flow is associated with a turbulent cascade to small scales? Two signs of a cascade forming in these calculations are that the velocity-derivative skewness S_u is nearly 0.5 in figure 3(*b*) and the total kinetic energy spectrum is about $k^{-5/3}$ for an intermediate range of wavenumbers in figure 5(*e*). The question of whether there is a cascade might hinge on the number of small velocity length scales in the flow. Herring (1966) has shown that a Kolmogorov energy spectrum would be consistent with only one boundary layer depth for both velocity and temperature. In addition to the thermal boundary layer thickness λ_T, two velocity scales have been identified, λ_u and z^*, neither of which scales as the Kolmogorov length scale η (4.2); η, the only small scale assumed if there is a cascade, would be a third small length scale, with $\beta_\eta = 9/28 = 0.32 > 2/7$.

Since there is more than one small scale, it would not be surprising to see effects contrary to one's expectations based upon cascade arguments. For example, for Prandtl number of the order of one, for passive scalars in isotropic turbulence the only spectral regimes expected for both velocity and temperature are $k^{-5/3}$ and an exponentially decaying high-wavenumber end. Instead, the temperature fluctuation spectrum decreases as k^{-1} in figure 5(*f*). This is consistent with the laboratory measurements of Deardorff & Willis (1985). It is also usually assumed that a turbulent cascade leads to isotropic small scales. The visualizations in §7 show strongly anisotropic structures which extend vertically across the box with horizontal dimensions down to the smallest length scales of the flow.

The numerical temperature fluctuation spectra are consistent with experimental frequency spectra in the sense that both these numerical spectra and experimental spectra are significantly less steep than $-5/3$. To explain the leading-order $\omega^{-7/5}$ experimental result of Sano *et al.* (1989), Castaing *et al.* (1989) invoke stratified arguments from Bolgiano (1959). Yakhot (1992) predicts the same result via different arguments. Complementary to the theoretical prediction for temperature spectra is a prediction of energy spectra going as $-11/5$, steeper than $-5/3$. Let us consider some of the assumptions and the evidence from the observations, then list several alternative explanations for the dynamics that might lead us to new insight in reconciling the inconsistencies between results consistent with homogeneous turbulence and the

strongly inhomogeneous properties that are required to produce the boundary layers, boundary layers that appear to be needed to produce the observed deviations from classical heat flux scaling.

First, there is experimental support for stratification in water tank convection experiments, that is a stable, inverse temperature gradient across the centre of the box. But the only attempt to experimentally measure wavenumber spectra directly, by Deardorff & Willis (1985), would support these numerical results, that is energy spectra going as $-5/3$ even while the temperature spectrum is less steep. A contradictory observation is that velocity fluctuations scale as $u(l) \sim l^{3/5}$ (Tong & Shen 1992), which is equivalent to a $-11/5$ energy spectrum. Another approach to explaining temperature fluctuation spectra less steep than $k^{-5/3}$ would be to assume that temperature fluctuations are created at all scales, which would be consistent with the strongly anisotropic structures seen and might still allow a $-5/3$ energy spectrum. It could also be argued that temperature spectra less steep than $-5/3$ are not surprizing since, with the possible exception of Kaimal *et al.* (1976), the experimental evidence for a $k^{-5/3}$ temperature variance spectrum has not been strong (Champagne *et al.* 1977; Sreenivasan 1991). It should also be noted that most of the experiments are in water with a higher Prandtl number than these simulations and ongoing simulations of variable Prandtl number (Kerr *et al.* 1995) leave open the possibility of different dynamics at different Prandtl numbers. These new calculations might also determine the origin of some of the differences in the large-scale structure, in particular that there is diagonal alignment and a dominant recirculating pattern is not observed here.

While the secondary scaling exponents summarized in table 1 agree with aspects of the theories of both Castaing *et al.* (1989) and Shraiman & Siggia (1990), the differences noted here, in experiments and in two-dimensional simulations (Werne *et al.* 1991), seem consistent in ways suggesting that they are true differences with the theoretical predictions that are more than logarithmic corrections (Shraiman & Siggia). In addition to confirming that the exponent ϵ in (2.1) is closer to $1/2$ than either the hard turbulence or classical predictions, these calculations also find a new type of temperature scaling at the top of the thermal boundary layer, $\Delta_w \sim Ra^{-1/14}$. $\epsilon > 3/7$ poses several problems for the theoretical relations outlined in §4. If $\epsilon > 3/7$ and $\beta_T = 2/7$, then (2.5) cannot be satisfied; and if $\epsilon > 3/7$, $\gamma = -1/7$, and $\beta_T = 2/7$, (2.6) is not satisfied. These are relatively minor differences with the theoretical assumptions that a more complete theory that also explains the anamolous spectra and structures would hopefully account for.

The support of ARO MIPR No. 103-86 at the National Center for Atmospheric Research (NCAR) is acknowledged. NCAR is sponsored by the National Science Foundation. The assistance of W. S. Wu in developing the code and doing the first calculations to show the feasibility of reaching the hard turbulence regimes is appreciated as well as discussions with J. R. Herring, C. H. Moeng, E. D. Siggia and J. Werne.

REFERENCES

ADRIAN, R. J., FERREIRA, R. T. D. S. & BOBERG, T. 1986 Turbulent thermal convection in wide horizontal fluid layers. *Exps. Fluids* **4**, 121–141.

BALACHANDAR, S. & SIROVICH, L. 1991 Probability distribution functions in turbulent convection. *Phys. Fluids* A **3**, 919–927.

BATCHELOR, G. K. 1969 Computation of the energy spectrum in homogeneous two-dimensional turbulence. *Phys. Fluids Suppl.* II **12**, 233–239.

BOLGIANO, R. 1959 Turbulent spectra in a stably stratified atmosphere. *J. Geophys. Res.* **64**, 2226–2229.

BUSSE, F. H. & WHITEHEAD, J. A. 1974 Oscillatory and collective instabilities in large Prandtl number convection. *J. Fluid Mech.* **66**, 67–79.

CASTAING, B., GUNARATNE, G., HESLOT, F., KADANOFF, L., LIBCHABER, A., THOMAE, S., WU, X. Z., ZALESKI, S. & ZANETTI, G. 1989 Scaling of hard thermal turbulence in Rayleigh-Bénard convection. *J. Fluid Mech.* **204**, 1–30.

CHAMPAGNE, F. H., FRIEHE, C. A., LARUE, J. C. & WYNGAARD, J. C. 1977 Flux measurements, flux estimation techniques, and fine-scale turbulence measurements in the unstable surface layer over land. *J. Atmos. Sci.* **34**, 515–530.

CHANDRASEKAR, S. 1961 *Hydrodynamic and Hydromagnetic Stability*. Clarendon.

CHU, T. Y. & GOLDSTEIN, R. J. 1973 Turbulent convection in a horizontal layer of water. *J. Fluid Mech.* **60**, 141–159.

CURRY, J. C., HERRING, J. R., LONCARIC, J. & ORSZAG, S. A. 1984 Order and disorder in two- and three-dimensional Bénard convection. *J. Fluid Mech.* **147**, 1–38.

DEARDORFF, J. W. 1970 Convective velocity and temperature scales for the unstable planetary boundary layer and for Rayleigh-Bénard convection. *J. Atmos. Sci.* **27**, 1211–1213.

DEARDORFF, J. W. & WILLIS, G. E. 1967 Investigation of turbulent thermal convection between horizontal plates. *J. Fluid Mech.* **28**, 675–704.

DEARDORFF, J. W. & WILLIS, G. E. 1985 Further results from a laboratory model of the convective planetary boundary layer. *Boundary-Layer Met.* **32**, 205–236.

DELUCA, E. E., WERNE, J., ROSNER, R. & CATTANEO, F. 1990 Numerical simulations of soft and hard turbulence: preliminary results for two-dimensional convection. *Phys. Rev. Lett.* **64**, 2370–2373.

DOMARADZKI, J. A. & METCALFE, R. W. 1988 Direct numerical simulations of the effects of shear on turbulent Rayleigh-Bénard convection. *J. Fluid Mech.* **193**, 499–531.

EIDSON, T. M., HUSSAINI, M. Y. & ZANG, T. A. 1986 Simulation of the turbulent Rayleigh-Bénard problem using a spectral/finite difference technique. *ICASE Rep.* 86-6. Also in *Direct and Large Eddy Simulation of Turbulence* (ed. U. Schumann & R. Friedrich), pp. 188–209. Vieweg, 1986.

FIEDLER, B. H. & KHAIROUTDINOV, M. 1994 Cell broadening in three-dimensional thermal convection between poorly conducting boundaries: large eddy simulations. *Beitr. Phys. Atmos.* **67**, 235–241.

GRÖTZBACH, G. 1982 Direct numerical simulation of laminar and turbulent Bénard convection. *J. Fluid Mech.* **119**, 27–53.

GRÖTZBACH, G. 1983 Spatial resolution requirement for direct numerical simulation of Rayleigh-Bénard convection. *J. Comput. Phys.* **49**, 241–264.

HERRING, J. R., 1966 Some analytic results in the theory of thermal convection. *J. Atmos. Sci.* **23**, 672–677.

HERRING, J. R. & KERR, R. M. 1982 Comparison of direct numerical simulations with predictions of two-point closures for isotropic turbulence convecting a passive scalar. *J. Fluid Mech.* **118**, 205–219.

HESLOT, F., CASTAING, B. & LIBCHABER, A. 1987 Transition to turbulence in helium gas. *Phys. Rev.* A **36**, 5870–5873.

KAIMAL, J. C., WYNGAARD, J. C., HAUGEN, D. A., COTÉ, O., IZUMI, Y., CAUGHEY, S. J. & READINGS, C. J. 1976 Turbulence structure in the convective boundary layer. *J. Atmos. Sci.* **33**, 2152–2169.

KERR, R. M. 1985 Higher-order derivative correlations and the alignment of small-scale structures in isotropic numerical turbulence. *J. Fluid Mech.* **153**, 31–58.

KERR, R. M. 1991 Velocity, scalar and transfer spectra in numerical turbulence. *J. Fluid Mech.* **211**, 309–332.

KERR, R. M, HERRING, J. R. & BRANDENBURG, A. 1995 Large-scale structure in Rayleigh-Bénard convection with impenetrable side-walls. *Chaos, Solitons and Fractals* **5**, 2047–2053.

KIM, J., MOIN, P. & MOSER, R. 1987 Turbulence statistics in fully developed channel flow at low Reynolds number. *J. Fluid Mech.* **177**, 133–166.

KRAICHNAN, R. H. 1967 Inertial ranges in two-dimensional turbulence. *Phys. Fluids* **10**, 1417–1423.

KRISHNAMURTI, R. 1995 Low frequency oscillations in turbulence convection: laboratory experiments. *Fluid Dyn. Res.* (in press).

KRISHNAMURTI, R. & HOWARD, L. N. 1981 Large-scale flow generation in turbulent convection. *Proc. Nat. Acad. Sci.* **78**, 1981–1985.

LENSCHOW, D. H., WYNGAARD, J. C. & PENNELL, W. T. 1980 Mean-field and second-moment budgets in a baroclinic, convective boundary layer. *J. Atmos. Sci.* **37**, 1313–1326.

MASON, P. J. 1989 Large eddy simulation of a convective atmospheric boundary layer. *J. Atmos. Sci.* **46**, 1492–1516.

MCLAUGHLIN, J. B. & ORSZAG, S. A. 1982 Transition from periodic to chaotic thermal convection. *J. Fluid Mech.* **122**, 123–142.

MÉTAIS, O. & LESIEUR, M. 1992 Spectral large-eddy simulation of isotropic and stably stratified turbulence. *J. Fluid Mech.* **239**, 157–194.

MOENG, C. H. & ROTUNNO, R. 1990 Vertical-velocity skewness in the buoyancy-driven boundary layer. *J. Atmos. Sci.* **47**, 1149–1162.

MOENG, C. H. & WYNGAARD, J. C. 1988 Spectral analysis of large-eddy simulations of the convective boundary layer. *J. Atmos. Sci.* **45**, 3573–3587.

MOSER, R. D., MOIN, P. & LEONARD, A. 1983 A spectral numerical method for the Navier-Stokes equations with application to Taylor-Couette flow. *J. Comput. Phys.* **52**, 524–544.

PRANDTL, L. 1932 Meteorologische Anwendungen der Strömungslehre. *Beitr. Phys. Atmos.* **19**, 188–202.

PRIESTLEY, C. H. B. 1954 Convection from a large horizontal surface. *Austral. J. Phys.* **7**, 176–201.

SANO, M., WU, X. Z., & LIBCHABER, A. 1989 Turbulence in helium-gas free convection. *Phys. Rev.* A **40**, 6421–6430.

SCHMIDT, H. & SCHUMANN, U. 1989 Coherent structure of the convective boundary layer derived from large-eddy simulations. *J. Fluid Mech.* **200**, 511–562.

SHE, Z. S. 1989 On the scaling laws of thermal turbulent convection. *Phys. Fluids* A **1**, 911–913.

SHRAIMAN, B. I. & SIGGIA, E. D. 1990 Heat transport in high-Rayleigh-number convection. *Phys. Rev.* A **42**, 3650–3653.

SIROVICH, L., BALACHANDAR, S. & MAXEY, M. R. 1989 Simulations of turbulent thermal convection. *Phys. Fluids* A **1**, 1911–1914.

SPALART, P. R. 1988 Direct simulation of a turbulent boundary layer up to $R_\theta = 1410$. *J. Fluid Mech.* **187**, 61–98.

SPALART, P. R., MOSER, R. D. & ROGERS, M. M. 1991 Spectral methods for the Navier-Stokes equations with one infinite and two periodic directions. *J. Comput. Phys.* **96**, 297–324.

SREENIVASAN, K. R. 1991 On local isotropy of passive scalars in turbulent shear flows. *Proc. R. Soc. Lond.* A **434**, 165–182.

THUAL, O. 1992 Zero Prandtl number convection *J. Fluid Mech.* **240**, 229–258.

TONG, P. & SHEN, Y. 1992 Relative velocity fluctuations in turbulent Rayleigh-Bénard convection. *Phys. Rev. Lett.* **69**, 2066–2069.

VINCENT, A. & MENEGUZZI, M. 1991 The spatial structure and statistical properties of homogeneous turbulence. *J. Fluid Mech.* **225**, 1–20.

WERNE, J. 1993 Structure of hard-turbulent convection in two dimensions: Numerical evidence. *Phys. Rev.* E **48**, 1020–1035.

WERNE, J., DELUCA, E. E., ROSNER, R. & CATTANEO, F. 1991 Development of hard-turbulent convection in two dimensions: Numerical evidence. *Phys. Rev. Lett.* **67**, 3519–3522.

WILLIS, G. E. & DEARDORFF, J. W. 1974 A laboratory model of diffusion into the convective planetary boundary layer. *Q. J. R. Met. Soc.* **102**, 427–445.

WU, X.-Z., KADANOFF, L., LIBCHABER, A. & SANO, M. 1990 Frequency power spectrum of temperature fluctuations in free convection. *Phys. Rev Lett.* **64**, 2140–2143.

WU, X.-Z. & LIBCHABER, A. 1992 Scaling relations in thermal turbulence: The aspect-ratio dependence. *Phys. Rev.* A **45**, 842–845.

WYNGAARD, J. C. & WEIL, J. C. 1991 Transport asymmetry in skewed turbulence. *Phys. Fluids* A **3**, 155–162.

YAKHOT, V. 1992 The 4/5-Kolmogorov law for statistically stationary turbulence. Application to high Rayleigh number Bénard convection. *Phys. Rev. Lett.* **69**, 769–771.

ZOCCHI, G., MOSES, E. & LIBCHABER, A. 1990 Coherent structures in turbulent convection, an experimental study. *Physica* **166A**, 387–407.